Insights into magmatic processes at Shishaldin Volcano based on satellite and airborne volcanic gas measurements and magma degassing models

Taryn Lopez, University of Alaska Fairbanks Geophysical Institute, Alaska Volcano Observatory, 0000-0001-6831-4573
Allan Lerner, U.S. Geological Survey, Cascades Volcano Observatory, Vancouver, WA, USA, 0000-0001-7208-1493.
Bruno Franco, Université libre de Bruxelles (ULB), BLU–ULB research Center, Spectroscopy, Quantum Chemistry and Atmospheric Remote Sensing (SQUARES), Brussels, Belgium, 0000-0003-0736-458X
Matthew W. Loewen, U.S. Geological Survey, Alaska Volcano Observatory, Anchorage, Alaska, 0000-0002-5621-285X
Peter Kelly, U.S. Geological Survey, Cascades Volcano Observatory, Vancouver, WA, USA, 0000-0002-3868-1046
Christoph Kern, U.S. Geological Survey, Cascades Volcano Observatory, Vancouver, WA, USA, 0000-0002-8920-5701
Laura Clor, U.S. Geological Survey, Cascades Volcano Observatory, Vancouver, WA, USA, 0000-0003-2633-5100.
Cynthia Werner, U.S. Geological Survey (contractor), New Plymouth, New Zealand, 0000-0003-3311-6694.
Lieven Clarisse, Université libre de Bruxelles (ULB), BLU–ULB research Center, Spectroscopy, Quantum Chemistry and Atmospheric Remote Sensing (SQUARES), Brussels, Belgium, 0000-0002-8805-2141
Daniel Rasmussen, Peregrine Advisors, Silver Spring, MD, USA, 0000-0003-0137-6715
Valerie Wasser, University of Alaska Fairbanks Geophysical Institute, Alaska Volcano Observatory, 0000-0001-9786-9770
Skye Kushner, University of Alaska Anchorage, Anchorage, Alaska, 0000-0002-7230-2185
Pablo Saunders-Shultz, U.S. Geological Survey, Alaska Volcano Observatory, Anchorage, Alaska, 0009-0009-4096-9821
Israel Brewster, University of Alaska Fairbanks Geophysical Institute, Alaska Volcano Observatory, Anchorage, Alaska
Nicolas Theys, Royal Belgian Institute for Space Aeronomy (BIRA-IASB), Brussels, Belgium, 0000-0002-3931-2429
Pavel Izbekov, University of Alaska Fairbanks Geophysical Institute, Alaska Volcano Observatory, 0000-0001-9052-7655

Corresponding Author: Taryn Lopez, tmlopez@alaska.edu

This manuscript is currently in review in the Bulletin of Volcanology.

Author Contributions:
Conceptualization: Taryn Lopez, Matt Loewen, Allan Lerner, Peter Kelly; Methodology: Taryn Lopez, Allan Lerner, Matt Loewen, Israel Brewster, Bruno Franco, Lieven Clarisse, Peter Kelly, Christoph Kern, Laura Clor, Dan Rasmussen, Nicolas Theys, Pavel Izbekov; Airborne gas data collection: Allan Lerner, Matt Loewen, Cindy Werner, Christoph Kern; TROPOMI data analysis during real-time AVO operations Taryn Lopez, Valerie Wasser, Skye Kushner, Pablo Saunders-Shultz; IASI data analysis: Bruno Franco, Lieven Clarisse; Degassing modeling and petrologic analysis: Allan Lerner, Dan Rasmussen, Peter Kelly, Pavel Izbekov; Writing - original draft preparation: Taryn Lopez; Writing - review and editing: Allan Lerner, Matt Loewen, Bruno Franco, Lieven Clarisse, Nicolas Theys, Peter Kelly, Christoph Kern, Cindy Werner, Valerie Wasser, Dan Rasmussen. All authors read and approved this manuscript submission.

Abstract:
Shishaldin Volcano is a remote and frequently active basaltic volcano with eruptions in 2019–2020 and 2023 that exhibited notable variations in monitoring signals and explosivity. Here we combine complementary ultraviolet (TROPOMI) and infrared (IASI) satellite SO_2 observations with airborne gas measurements, petrologic constraints, and degassing models to investigate magma degassing processes and quantify SO_2 emissions during these recent eruptions. Cumulative SO_2 emissions differed by an order of magnitude between the 2019–2020 and 2023 eruptions (~40 vs ~240 kt), and SO_2 emission rates spanned a wide range (<100 to ~85,000 t/d) over the 5-year study period, indicating highly variable magma supply rates. SO_2 plumes are almost exclusively observed from satellites during or following volcanic unrest and eruption, indicating substantial SO_2 degassing from magma at relatively shallow depths, consistent with degassing models. Airborne CO_2/SO_2 gas ratios of 1–2 measured during 2019—2020 and following the 2023 eruptions correspond to relatively shallow (<2–4 km) magma degassing depths, while a ratio of ~11 measured between these eruptions corresponds to magma degassing at >12 km depths. Collectively, these observations indicate that while exsolved volatiles can separate from their host magma, consistent with open-system degassing in the upper crust, most SO_2 is released during eruption. We hypothesize that magma ascent rates control Shishaldin Volcano's degassing behavior and eruption style, with lower magma fluxes enabling open-system degassing and quiescent to weakly explosive eruptions, and higher fluxes producing closed-system degassing and highly explosive eruptions. These results demonstrate that satellite SO_2 observations can successfully track magma supply to the shallow crust and if acquired at sufficient temporal resolution SO_2 observations may provide advanced warning of impending paroxysms.

1.1 Introduction:

Volcanic gas emissions are a key monitoring metric used by volcano observatories to infer subsurface conditions and inform volcano monitoring and eruption warnings. Exsolved volatiles such as water (H_2O), carbon dioxide (CO_2) and sulfur dioxide (SO_2) can separate from their host magma due to their relatively low density, and if permeable pathways exist, ascend through a volcanic conduit and outgas at Earth's surface (e.g., Edmonds and Woods, 2018). This provides information that can be used to infer subsurface processes. The unique solubility controls of each volatile species in magma allow these volatiles to exsolve at different depths, such that the ratio of soluble to insoluble volatiles can provide insights into magma degassing depth (Giggenbach, 1996; Burton et al., 2007). Furthermore, the total output (emission rate or flux) of volcanic gases at the surface can provide insights into the quantity of magma degassing in the subsurface and controls on volatile outgassing such as conduit permeability (e.g., Gerlach et al., 1994; Edmonds et al., 2003a; Aiuppa et al., 2008; Shinohara et al., 2008). With this information scientists can use volcanic gas emissions data to monitor changes in magma degassing, track magma intrusion and ascent, and help forecast volcanic eruptions (e.g., Aiuppa et al., 2007; Burton et al., 2007; Werner et al., 2013, de Moor et al., 2016).

Due to its low background concentration in unpolluted air, SO_2 is the easiest and most measured major volcanic gas species (Oppenheimer et al., 2011). Its unique absorption of ultraviolet (UV) and infrared (IR) radiation enables SO_2 to be measured using ground-based, airborne, and satellite remote sensing techniques (Kern et al., 2025). Remote sensing enables SO_2 emissions to be quantified over space and time, making these techniques well-suited for detecting changes in volcanic emissions (e.g., Quieber et al., 2019; Burton et al, 2021; Kern et al., 2020; Esse et al., 2025a, b).

In the past, routine monitoring of relatively low quantities of volcanic SO_2 emissions was only possible using ground-based techniques (e.g., Galle et al., 2003; Edmonds et al., 2003b; Arellano et al., 2022). This changed with the 2017 launch of the hyperspectral TROPOspheric Monitoring Instrument (TROPOMI) UV sensor aboard the Sentinel 5P satellite. Thanks to TROPOMI's substantially higher spatial resolution relative to predecessor satellites, and the high sensitivity to SO_2 afforded by UV sensors, TROPOMI can detect SO_2 emission rates as low as ~100–200 metric tons per day (t/d) under optimal measurement conditions (Theys et al., 2019). One limitation of UV sensors such as TROPOMI is their dependence on scattered sunlight as a radiation source, which results in a substantially reduced sensitivity in winter at high latitude locations, such as Alaska (Carn et al., 2013; Lopez et al., 2013).

Here we use observations of SO_2 emissions from the TROPOMI sensor that were used operationally by the Alaska Volcano Observatory (AVO) to monitor magmatic degassing during the 2023 Shishaldin Volcano eruption. We combine these observations with retrospective analysis of: (a) TROPOMI data for the 2019–2020 Shishaldin Volcano eruption, and (b) complementary satellite SO_2 data from the Infrared Atmospheric Sounding Interferometer (IASI) sensors for both the 2019–2020 and 2023 eruptions to constrain a robust SO_2 degassing time series, as well as total cumulative SO_2 emission masses for these two eruptions. We then combine these satellite SO_2 observations with complementary airborne gas measurements, petrologic constraints, and magma degassing models to elucidate magma degassing processes, provide estimates of degassed magma volumes and magma fluxes, and suggest gas monitoring strategies to help forecast future Shishaldin Volcano eruptions.

1.2 Geologic Setting and Eruptive History:

Shishaldin Volcano (54.755°N, 163.971°W, 2858 m prior to the 2019 eruption) is a remote and frequently active stratovolcano on Unimak Island, Alaska. Its three most recently sampled eruptions in 1999, 2019–2020, and 2023 produced fairly homogenous basalts with ~49–50 wt.% SiO_2 (Nye et al., 2002; Stelling et al., 2002; Izbekov et al., 2027), though Pleistocene eruptions have also produced andesitic and dacitic lavas (Nye et al., 2002; Stelling et al., 2003; Loewen et al., 2026a). It is one of the most active volcanoes in Alaska, with over 40 historically documented eruptions since ~1700 (Nye et al., 2002), and at least seven eruptions in the past three decades including: 1995, 1997, 1999, 2004, 2013–2015, 2019–2020 and 2023. Recent eruptions resulted in lava flows, a short-lived summit lava lake, Strombolian explosions, lava fountaining, and sub-Plinian paroxysms. Prior to the 2023 eruption, the 1999 eruption was the most significant eruption of Shishaldin Volcano, consisting of two major explosive events, including a sub-Plinian eruption on 19 April 1999 that released a total of ~63 kt SO_2 (Nye et al., 2002; Carn et al., 2015). Eruptions sometimes occur with minimal detected precursory signals, making it difficult to forecast eruption onset. While Shishaldin Volcano is relatively remote, explosive eruptions can produce ash clouds that are hazardous to local populations (e.g., False Pass, population ~400, 30 km to the east (2020 Census)) and mariners, and produce a substantial aircraft hazard to the >60,000 passengers travelling across Alaska airspace each day (Ewert et al., 2018).

1.2.1 2019–2020 and 2023 Eruption Overviews:

Detailed chronologies of Shishaldin Volcano's 2019–2020 and 2023 eruptions are provided in Loewen et al. (2026a) and summarized here.

Shishaldin Volcano's 2019–2020 eruption took place between 24 July 2019 and 31 March 2020 (Loewen et al., 2026a). The eruption onset was preceded by ~2–3 weeks of elevated surface temperatures, long period seismicity, and seismic tremor and was detected when lava was seen in the summit crater during an overflight (Orr et al., 2023). Activity throughout this eruption was dominated by spatter cone growth within the summit crater, Strombolian explosions, and lava effusion. Activity became more explosive in January 2020, with lava fountaining and the occurrence of three ash-rich paroxysmal events that produced ash clouds that reached ~7–8 km above sea level (23,000–27,000 ft; Loewen et al., 2026a, Gomez-Patron et al., 2026). Low-level explosive activity resumed briefly in March 2020 but was confined to the ~200 m diameter summit crater (Orr et al., 2023; Waythomas et al., 2026). Activity declined and observations on 1 April confirmed that there was no lava at the surface marking the end of the eruption. Elevated surface temperatures and satellite SO_2 detections continued into May 2020 (Orr et al., 2024).

The 2023 eruption of Shishaldin Volcano occurred between 11 July and 13 November 2023 following three years of quiescence (Loewen et al., 2026a). The first potential sign of renewed Shishaldin Volcano unrest was intermittent seismic tremor seen in March 2023 (Fee et al., 2026) followed by a possible satellite SO_2 detection on 5 April 2023. Then in early July 2023 intermittent seismic tremor and low frequency earthquakes were detected approximately one week prior to the 11 July eruption onset. Unlike the 2019–2020 eruption, 2023 eruptive activity was largely explosive. A pattern of weakly explosive eruptive activity (e.g., Strombolian explosions) that transitioned into highly explosive eruptive activity or paroxysms (e.g., large Strombolian explosions or lava fountaining), that produced relatively high-altitude (~5–14 km, ~17,000-46,000 ft), ash-rich, eruption clouds, persisted over the next four months (Fee et al., 2026; Loewen et al., 2026a). Between July and November 2023, 13 paroxysmal eruptions (events) occurred, including: Event 1 (14 July), Event 2 (15 July), Event 3 (18 July), Event 4 (22 July), Event 5 (25 July), Event 6 (3 August), Event 7 (14 August; Fig. 1), Event 8 (25 August), Event 9 (5 September), Event 10 (15 September), Event 11 (22 September), Event 12 (3 October), and Event 13 (3 November; Loewen et al., 2023). The eruption ended immediately following Event 13 (Loewen et al., 2026a), though infrasound signals, elevated seismicity, surface temperatures, SO_2 emissions, and collapse events within the summit crater occurred over the following weeks. Activity gradually declined but remained above background for the first half of 2024.

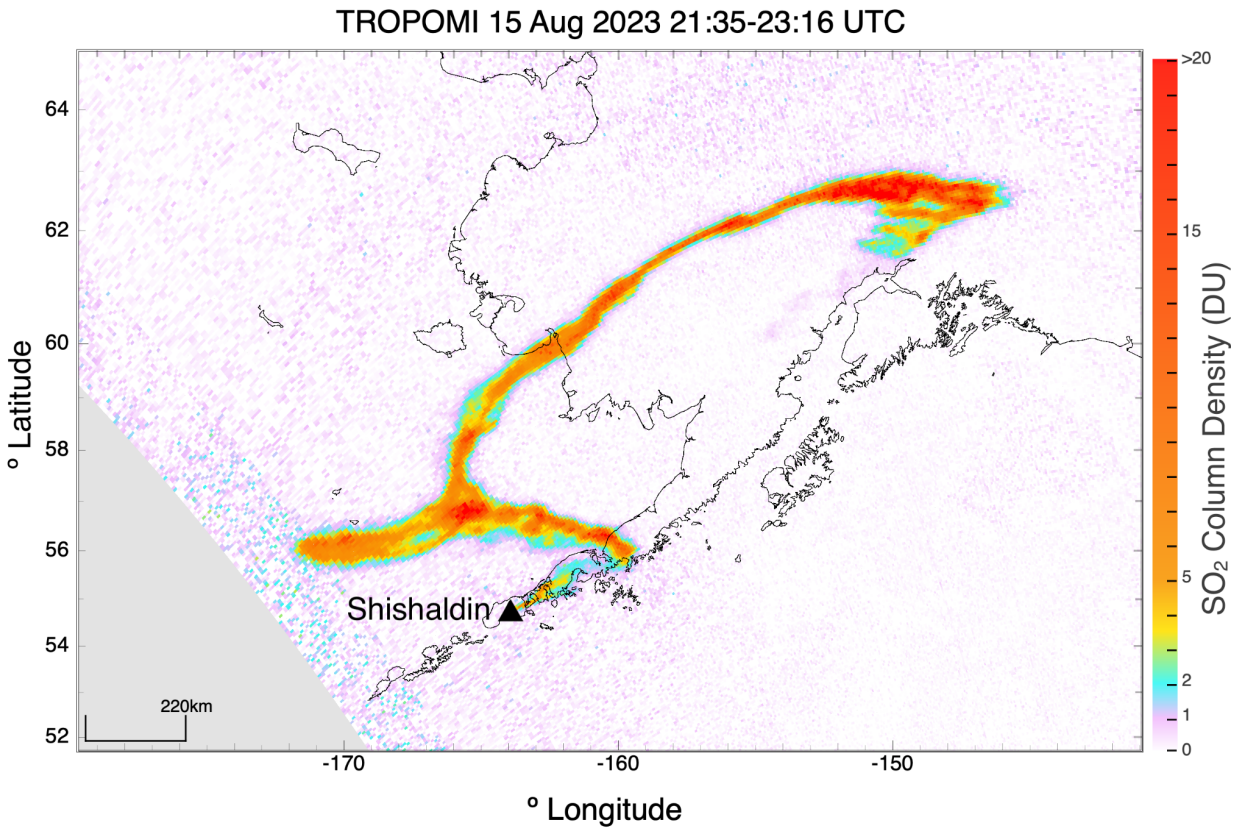


Figure 1: TROPOspheric Monitoring Instrument (TROPOMI) image acquired on 15 August 2023 at 21:35 UTC depicting the SO_2 plume produced during Event 7 of the 2023 eruption of Shishaldin Volcano (labeled triangle). This detection produced an SO_2 mass of 25.9 kilotons (kt). The color bar scale shows the SO_2 column density in Dobson Units (DU) based on the 7 km TROPOMI altitude product.

1.3 Monitoring by the Alaska Volcano Observatory:

Shishaldin Volcano is monitored by AVO using ground-based seismic stations, infrasound sensors, tiltmeters, Global Navigation Satellite System (GNSS) stations, and webcams. The local monitoring network is complemented by satellite observations to detect and quantify surface deformation using Synthetic Aperture Radar (SAR) and Interferometric Synthetic Aperture Radar (InSAR (Angarita et al., 2022; Angarita et al., 2026a); elevated surface temperatures and ash clouds using thermal remote sensing (Loewen et al., 2026a); and SO_2 emissions using the TROPOMI sensor (this study). Additionally, airborne gas in situ and remote sensing campaigns are conducted every 1 to 2+ years, as conditions permit, to measure SO_2 emission rates and plume gas composition (this study). Although infrequent, these airborne gas campaigns provide key geochemical context for interpreting the satellite SO_2 data and time series trends.

2. Methods:

2.1 Constraining SO_2 Masses and Emission Rates from Satellite

2.1.1 TROPOMI

Since 2020, AVO has been using TROPOMI data operationally to detect and quantify volcanic SO_2 emissions from Alaska volcanoes (Coombs et al., 2024, Lyons et al., 2025). TROPOMI provides better than daily global coverage at Alaska's high latitude with a nadir pixel resolution of 3.5 x 5.5 km^2 (as of August 2019; Theys et al., 2019). This is a ~16-fold increase in spatial resolution relative to the Ozone Monitoring Instrument (OMI), the previous best-available UV satellite sensor. TROPOMI measures UV solar radiation that is backscattered off Earth's atmosphere and calculates absorbance by volcanic SO_2 within an atmospheric column, with data here derived from the Differential Optical Absorption Spectroscopy (DOAS) algorithm (Theys et al., 2017). Comparisons with other operational satellite sensors SEVIRI (Spinning Enhanced Visible InfraRed Imager), MODIS (Moderate Resolution Imaging Spectroradiometer), VIIRS (Visible Infrared Imagine Radiometer Suite), TROPOMI, and AIRS (Atmospheric Infrared Sounder) show that TROPOMI is the most sensitive of those sensors for volcanic SO_2 monitoring, followed by the IR IASI sensor (Clarisse et al., 2026; Corradini et al., 2021). AVO's TROPOMI SO_2 emissions dataset provides continuous observations over a multiyear period to allow changes in degassing to be detected and to complement discrete airborne gas measurements.

Here we describe the TROPOMI data analysis methods used by AVO since June 2020 to monitor and quantify volcanic SO_2 emissions of Alaska volcanoes from space. TROPOMI near-real-time SO_2 data products with coverage of Alaska are pulled from the Sentinel Hub Catalog API (https://dataspace.copernicus.eu/analyse/apis/catalogue-apis) as they become available (~2 hours after overpass time). Image (png) files of TROPOM SO_2 Vertical Column Density (VCD) products in Dobson Units (DU, where 1 DU = 2.69 x 10^{20} molecules SO_2/m^2) and cloud coverage are created for five spatial sectors of the Aleutian-Alaska Arc and pushed to AVO's satellite image viewing platform, VolcView (Coombs et al., 2024). SO_2 images are generated for both the 1 km and 7 km TROPOMI altitude products, which assume plume masses centered at these altitudes, encompassing the most common range of plume heights for non-explosive activity in Alaska. Each morning an AVO Duty Remote Sensing analyst views all satellite imagery acquired over the past 24 hours and reports on any possible SO_2 detections. On a weekly basis (or daily during significant volcanic unrest) an AVO Duty SO_2 analyst: (a) reviews the past week's imagery and characterizes the detections as low-, medium-, and high-confidence; (b) calculates masses and emission rates for medium- and high-confidence detections; and (c) shares results using AVO's internal communications tools, and saves them to AVO's remote sensing database (Coombs et al., 2024).

We use the following criteria to characterize each plume detection: high-confidence detections depict an SO_2 signal in the vicinity of a known degassing or potentially restless volcano that visually exceeds the background noise over a ~1000 km spatial scale using a 0–20 DU color bar for both the 1 and 7 km altitude TROPOMI SO_2 products. High-confidence detections also have a distinct plume or cloud shape and provide agreement within 90° to reasonable backward wind trajectories to the source volcano. We consider reasonable plume altitudes to be ~6 km (~20,000 ft) or less for non-eruptive degassing (based on visual observations), and higher for explosive degassing. Medium-confidence detections are the same as high-confidence, except the SO_2 signal is only clearly above background in the 7 km altitude product. Low-confidence detections are those whose SO_2 signal only exceeds the noise level on a local, but not regional, scale in the 7 km altitude product, or it does not have a distinct plume or cloud shape, or the SO_2 source is questionable. Low-confidence detections may only contain a few elevated pixels and are considered possible detections, which may not be true volcanic signals or may be diffuse volcanic SO_2 from a potentially different (distal) source. While low-confidence detections are reported, no masses or emission rates are calculated for these observations. Figure 2 provides an example of a low- (a), and medium- (b) confidence detection from Shishaldin Volcano, while Figures 1 and 3 provide examples of high-confidence detections. Because the criteria and analysis software evolved over this five-year study period, all Shishaldin Volcano detections were reviewed and reanalyzed using our most recent criteria and software for this study, and to fill in any new observations from 2019 and early 2020.

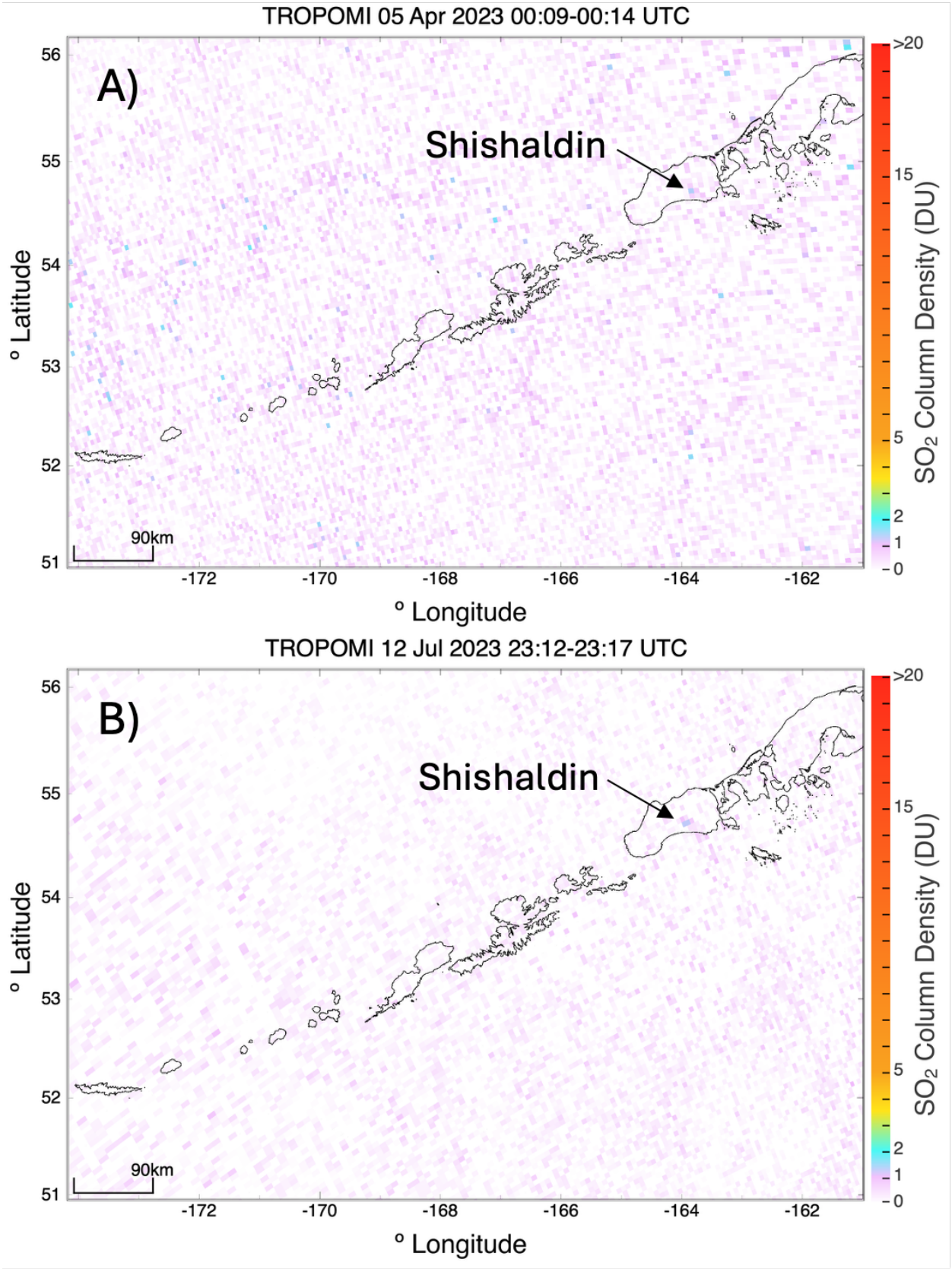

TROPOMI 05 Apr 2023 00:09-00:14 UTC
A)
Shishaldin
90km
56
55
54
53
52
51
-172
-170
-168
-166
-164
-162
° Latitude
° Longitude
>20
15
5
2
1
0
SO2 Column Density (DU)
TROPOMI 12 Jul 2023 23:12-23:17 UTC
B)
Shishaldin
90km
° Latitude
° Longitude
SO2 Column Density (DU)

Figure 2: Examples of (A) low- and (B) medium-confidence SO_2 detections as defined by the Alaska Volcano Observatory (AVO) based on the 7 km TROPOMI SO_2 altitude products. A) Example of a low-confidence SO_2 detection seen on 5 April 2023 following potential early precursory seismic unrest with plume pixels exceeding ~1 DU (dark purple to blue colors). B) Example of a medium-confidence detection seen on 12 July 2023 at the start of the 2023 eruption with a calculated emission rate of ~670 t/d.

SO_2 masses and emission rates are calculated using an in-house Python tool called SO_2 Explorer (https://bitbucket.org/ijbrewster/tropomi_gui/src/master/). For each medium- and high-confidence SO_2 detection the analyst manually selects the plume in the 7 km altitude product. The software automatically calculates the mass of the plume at each TROPOMI SO_2 altitude product (1, 7 and 15 km) by multiplying each plume pixel area (m^2) by the SO_2 VCD in units of g SO_2/m^2) and summing each pixel SO_2 mass to get a total plume SO_2 mass (reported in kilotons, kt; Fig. 3). This mass is then corrected for any systematic background offset by subtracting the median mass of four equal-area background polygons distributed in all cardinal directions around the detection area, and whose placement can be adjusted by the analyst as needed (Fig. 3b). Next, Global Data Assimilation System (GDAS) modeled wind data (https://www.ncei.noaa.gov/products/weather-climate-models/global-data-assimilation) are overlain onto the TROPOMI image starting from the farthest downwind plume pixel at the TROPOMI image overpass time. The SO_2 analyst selects either a single plume trajectory, or two bounding plume trajectories, that best match the plume shape to constrain plume height (Fig. 3c). Wind shear in the vertical profile of the atmosphere allows the plume's altitude to be estimated from its downwind propagation and the modeled wind data. When multiple trajectories provide a good match to plume shape, the trajectory closest to the summit altitude, the trajectory that provides the median emission rate, or the trajectory that best matches plume appearance is chosen, based on analyst discretion and/or other observational data available (e.g., webcam imagery). When no trajectory provides a good match to plume shape, no plume mass or emission rate are reported. The software then calculates: (a) an altitude-corrected plume mass by linearly interpolating between the two bounding TROPOMI altitude products (1, 7 and/or 15 km) to the identified plume height, and (b) the age of the plume in hours based on the transport time from the volcanic source to the selected downwind plume pixel. Finally, time-averaged SO_2 emission rates are calculated by dividing the altitude-corrected SO_2 mass by the plume age and converting the product to t/d.

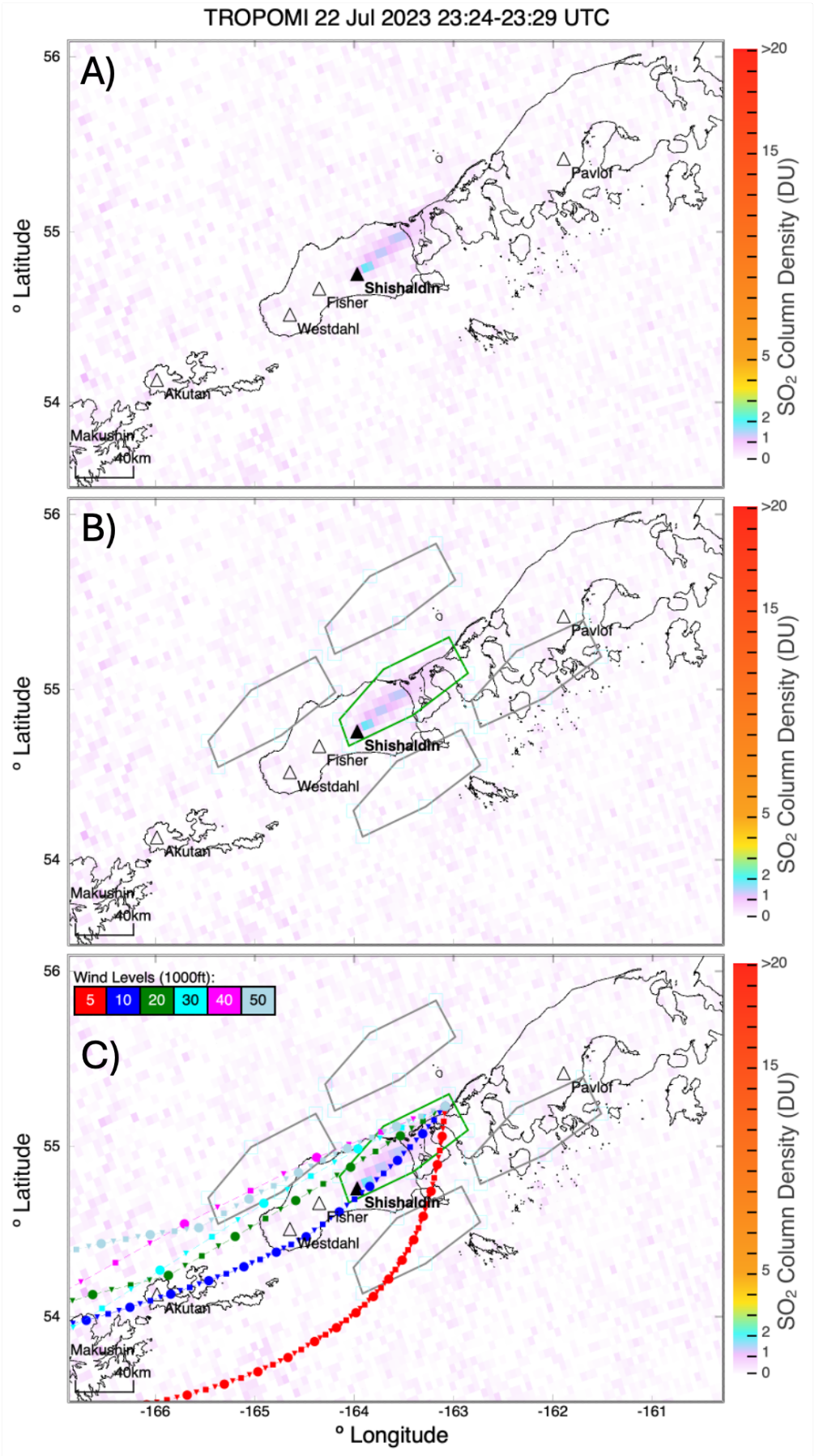

TROPOMI 22 Jul 2023 23:24-23:29 UTC
A)
B)
C)
Pavlof
Shishaldin
Fisher
Westdahl
Akutan
Makushin
40km
Wind Levels (1000ft):
5
10
20
30
40
50
° Latitude
° Longitude
56
55
54
-166
-165
-164
-163
-162
-161
SO2 Column Density (DU)
>20
15
5
2
1
0

Figure 3: Illustration of the analysis methods used to calculate SO_2 masses and emission rates from TROPOMI data. A) Example high-confidence SO_2 signal from Shishaldin Volcano seen on 22 July 2023 at 23:24 UTC, in the lead up to Event 4, approximately six hours before ash emissions were detected in satellite data. B) Example showing the selected plume polygon (green) and the adjacent equal-area background noise polygons (gray) used to do the background correction. C) Overlain wind trajectories from the Global Data Assimilation System (GDAS) model used to identify the best fitting plume trajectory (plume height, in this case 10,000 feet above sea level (ft asl, or 3.1 km) and plume age (~3.25 hours), to calculate the altitude-corrected plume SO_2 mass and emission rate (~290 t/d).

Here we estimate uncertainties in SO_2 plume mass of ±30%, a value less than the ±45% uncertainty calculated for satellite-derived SO_2 emission rates by Corradini et al. (2021) which also includes uncertainties in plume speed. We acknowledge that uncertainties in our calculated emission rates are higher but currently not well constrained. We report an emission rate precision to characterize the range in emission rate values based on the variability in plausible wind trajectory altitudes and plume ages. Here, high-precision emission rates show reasonable agreement (within 50%) between results calculated for the three plausible/bounding wind trajectory altitudes (typically 1.5, 3.0 and 6.1 km or 5000, 10,000 and 20,000 ft); while low precision emission rates yield differences >50%. We estimate uncertainties in high- and low-precision emission rates of <50% and >50%, respectively, similar to reported in Corradini et al. (2021). We also acknowledge that our SO_2 detections and calculated total emissions are likely to be underestimated due to the occasional presence of clouds located above a volcanic plume (Theys et al., 2017, 2019; Cotterill et al., 2024) and decreased UV in Alaska winters (Carn et al., 2011), both of which hinder detection of volcanic plumes. There is currently no method to accurately account for these missed detections, such that the total SO_2 emissions calculated here should be considered underestimates.

2.1.2 IASI

IASI is a series of three identical hyperspectral IR satellite sensors aboard the polar orbiting MetOp-A, -B and -C platforms (Clerbaux et al., 2009). IASI provides twice-daily global coverage with volcanic SO_2 products from 2007 through 2021 for MetOp-A and to the present for MetOp-B and -C (Clarisse et al., 2026). It is currently one of the most sensitive IR instruments for detecting and quantifying volcanic SO_2, owing to its relatively high pixel resolution (~12 km at nadir) and high spectral resolution (Corradini et al., 2021). Compared to UV sensors, IASI sensors can detect volcanic SO_2 emissions during nighttime and at high latitudes in winter (e.g., Lopez et al., 2020), but like other IR sensors, have lower sensitivity to low altitude SO_2 plumes due to the strong

interference from water vapor and reduced thermal contrast (Realmuto et al., 1994; Taylor et al., 2018). IASI has a lower spatial resolution than TROPOMI, with pixel areas ~7 times larger than TROPOMI at nadir. Therefore, combining TROPOMI and IASI provides more robust constraints on volcanic SO_2 emissions than is possible by either sensor alone, with TROPOMI being more sensitive to low-altitude, low concentration and spatially small plumes and IASI more effective in low UV winter and night conditions (Taylor et al., 2018).

The IASI SO_2 v4.5 dataset (Clarisse et al., 2026), which contains both SO_2 column densities and plume heights, was used to detect and quantify volcanic SO_2 emissions from Shishaldin Volcano through a multistep process. First, IASI overpasses covering the North Pacific were screened for any SO_2 detections over a specified region (180°W to 125°W, 45°N to 75°N). For flagged detections, SO_2 masses were calculated over both this large domain and a smaller domain centered on Shishaldin Volcano (172°W to 156°W, 50°N to 58°N). Each detection was then manually reviewed to confirm Shishaldin Volcano as the likely SO_2 source, and to refine the integration domain to include only SO_2 emissions from the past day. Finally, IASI detections were compared to the TROPOMI detections to identify signals missed in the initial IASI analysis, which were then reanalyzed for SO_2 mass and plume height using the methods above.

2.1.3 Integration of TROPOMI and IASI Observations

To compare IASI and TROPOMI observations we use the average SO_2 masses and plume heights derived from morning overpasses of the available IASI sensors and compare them with the best TROPOMI observation per local day. All three IASI instruments were operational for the 2019–2020 Shishaldin Volcano eruption, while only MetOp-B and -C were operational for the 2023 eruption. IASI morning overpasses generally occur ~0.25–3.33 hours before TROPOMI passes, making them well-suited for comparison. Because of the high latitude location of Shishaldin Volcano and TROPOMI's polar orbit, there are also commonly multiple TROPOMI observations per day. The "best" TROPOMI observation per day is determined by the analyst as the overpass with the most complete coverage of a volcanic plume, the highest signal to noise, and/or the best fit to modeled wind data. To minimize double counting of the same plume SO_2 signal we: (a) exclude evening IASI detections, and (b) manually filter residual SO_2 from previous days when identifiable, based on wind trajectory information and/or the diffuse nature of the SO_2 signal for both TROPOMI and IASI observations. Once the best observations per day have been identified, we merge the TROPOMI and IASI observations into a single data table (Table S.1). Next, we identify all morning IASI SO_2 detections that occurred within the 3.33 hours preceding a TROPOMI detection (the maximum time difference between TROPOMI and IASI morning overpasses). If Shishaldin Volcano SO_2 observations were made by both TROPOMI and IASI within

3.33 hours of each other, we consider it a matched detection and directly compare the two observations.

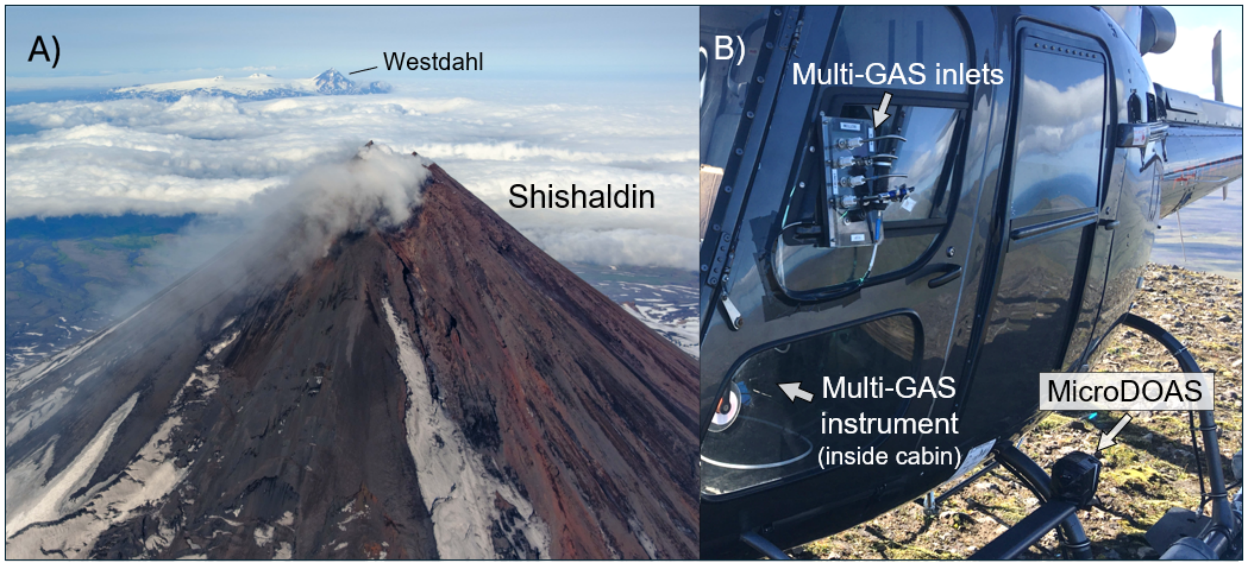


Figure 4: (A) View of Shishaldin Volcano from the northeast prior to the 30 July 2024 gas flight showing a typical post-2023 eruption degassing plume and the summit crater crack. For scale, the summit crater is ~200 m across. (B) Photo of the 4 Sep 2020 gas flight instrumentation showing a typical setup for AVO gas flights, including a multi-GAS (multicomponent Gas Analyzing System) instrument within the helicopter cabin, an airborne inlet attached to the passenger side window to pull gases into the multi-GAS instrument, and a micro Differential Optical Absorption Spectrometer (DOAS) instrument taped to the passenger-side helicopter step. AVO/U.S. Geological Survey (USGS) images from M. Loewen (#195819, https://mmdb.avo.alaska.edu/view/195819) and A. Lerner (#197210, https://mmdb.avo.alaska.edu/view/197210) with AVO Multimedia Database numbers and links provided.

2.2 Gas Composition and Emission Rates from Airborne Gas Flights

Seven helicopter-based airborne gas flights were conducted by U.S. Geological Survey (USGS) and/or AVO personnel at Shishaldin Volcano between 2015–2024 (Alaska Volcano Observatory, 2026) that can provide degassing context prior to, during, and following our satellite SO_2 dataset (2019–2023). During these gas flights, plume gas composition measurements of H_2O, CO_2, SO_2 and H_2S were made using an in situ portable multi-GAS (multicomponent Gas Analyzer System) instrument (e.g. Aiuppa et al., 2005) while flying through the volcanic plume, and measurements of overhead plume SO_2 column density were made using a micro Differential Optical Absorption Spectrometer (microDOAS) instrument (Kern, 2025) while flying below the plume to

calculate SO_2 emission rates (Fig. 4). Wind speed was measured at summit plume altitude following the windcircle approach (e.g., Doukas et al., 2002). Most gas flights consisted of ~5 plume intercepts for gas composition constraints, and a similar number of below-plume orbits for emission rate calculations.

The multi-GAS instruments used here contained either a LI-COR 840 or PP Systems SBA-5 gas analyzer for measuring H_2O and CO_2, and electrochemical sensors for quantifying SO_2 (City Technologies T3ST/F, 0−200 ppm range) and H_2S (City Technologies T3H, 0−100 ppm range). The gas sensors were integrated with a Garmin Global Positioning System (GPS) 18x receiver and a Campbell Scientific data logger (either CR1000 or CR300) into a small, field-portable package. The airborne measurements were processed using techniques described previously (Kelly et al., 2013, Werner et al., 2017; 2020). The gas sensor responses were checked before and after each field campaign and were accurate within 15%.

The microDOAS instruments used here consist of an Ocean Optics miniature grating spectrometer (USB 2000+ or FLAME-S model), zenith-pointing telescope, integrated GPS receiver, and a single-board computer that runs the measurements (BeagleBone Black; Kern, 2025). During the field campaign and under plume-free conditions, dark and clear sky measurements are acquired. SO_2 VCD measurements of the overhead plume were made by flying half-orbits around the volcano and on the down-wind side of the edifice to acquire full spatial coverage of the volcanic plume. Following the campaigns, microDOAS spectral data were analyzed for SO_2 VCD using the DOASIS fit routines (Kraus, 2006) in the 310−340 nm wavelength range and following the standard DOAS method (Platt and Stutz, 2008). SO_2 measurements were then analyzed spatially to derive emission rates by integrating the SO_2 VCDs over the plume width and multiplying the product by the perpendicular component of the plume speed to get an SO_2 emission rate (Galle et al., 2003). The SO_2 emission rates were then combined with the measured molar gas ratios relative to SO_2, as determined from multi-GAS data, to calculate total volatile emission rates (e.g., Gerlach et al., 1998).

3. Results:

3.1 Satellite SO_2 Observations

3.1.1. TROPOMI

Between 2019 and 2023, SO_2 emissions from Shishaldin Volcano were detectable by TROPOMI on 104 occasions, including 19 low-, 37 medium-, and 48 high-confidence detections. For all 85 medium- and high-confidence detections with acceptable (within 90°) fits to modeled wind trajectories, SO_2 masses and emission rates were calculated (Figs. 5, 6). These results can be found in Loewen et al. (2026) and Table S.2. SO_2

emissions over the study period were highly variable with masses and emission rates varying by four orders of magnitude. SO_2 masses ranged from 0.005 to ~35 kt, with calculated SO_2 emission rates ranging from <100 t/d to ~85,000 t/d. Variations in SO_2 plume character were substantial, with plume ages from 0.25 to 27 hours, plume lengths from 14 to ~4300 km, and plume heights from 1.5 to 12.2 km. The cumulative SO_2 mass released by Shishaldin Volcano over the five-year study period as detected by TROPOMI (calculated as the sum of all mass detections) is 267 kt.

Table 1: Satellite SO_2 Observations for Shishaldin Volcano's 2019–2020 and 2023 Eruptions

	Minimum	Median	Maximum	Number	Standard Deviation	Cumulative
2019-2020						
SO_2 Mass (kt)						
TROPOMI	0.005	1.11	15.29	28	3.22	31.2
IASI	0.05	0.194	6.22	20	1.68	15.7
SO_2 Emission Rate (t/d)						
TROPOMI	<100	435	25,033	28	7477	-
2023						
SO_2 Mass (kt)						
TROPOMI	0.005	0.74	34.73	57	8.22	235.7
IASI	0.13	1.09	25.14	28	6.63	108.1
SO_2 Emission Rate (t/d)						
TROPOMI	<100	2382	84,595	56	19,454	-

Based on data from Loewen et al. (2026) and Table S.2.

Notable differences were seen in SO_2 emissions between the 2019–2020 and 2023 eruptions. First, more than twice as many medium- and high-confidence Shishaldin Volcano SO_2 detections were made in 2023 (n=57) relative to 2019–2020 (n=28). Also, while lower quantities of SO_2 masses and emission rates were similar for the two eruptions, consistent with instrumental detection limits, median and maximum values for the 2023 eruption were notably higher (Table 1). Finally, the cumulative TROPOMI derived SO_2 mass for the 2023 eruption (235.7 kt) was 7x larger than that of the 2019–2020 eruption (31.2 kt). To eliminate the possibility that a substantial quantity of

Shishaldin Volcano SO_2 went unquantified by TROPOMI during winter for the 2019–2020 eruption, we next compare our observations with IASI.

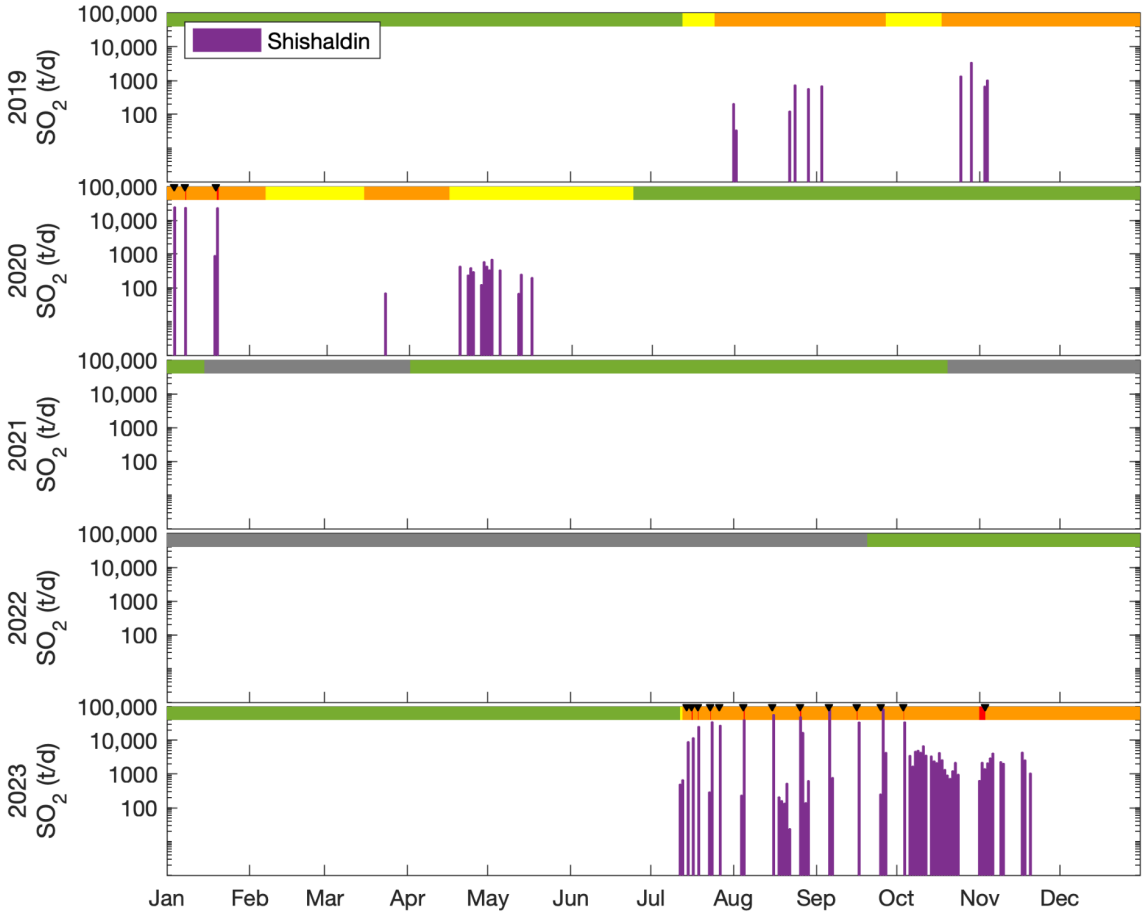


Figure 5: Five years of TROPOMI derived SO_2 emission rates (purple bars) from 2019 (top) through 2023 (bottom) plotted on a logarithmic scale. AVO's Aviation Color Code (Gardner and Guffanti, 2006) is plotted on the top of each figure reflecting AVO's public notices about volcano status, which we use here as a proxy for volcanic activity, acknowledging that this by nature sometimes lags volcanic activity. Here green represents background activity, yellow indicates above background activity, orange indicates an eruption is underway or imminent, red indicates that a substantial explosive eruption is underway or imminent, and gray indicates the monitoring network is impaired such that activity cannot be accurately characterized. Black triangles on the top of each plot mark major explosive events as identified by AVO (Loewen et al., 2026b).

3.1.2. IASI

During the two eruptive periods, SO_2 detections were made on 48 days from the various IASI sensors (Fig. 6, Table S.3). Retrieved IASI-derived SO_2 masses ranged from 0.05

to 25.14 kt, with plume heights between 3 and 11.4 km. The cumulative IASI-derived SO_2 mass over the full analysis period yields 123.8 kt. As with TROPOMI, there are notable differences seen in IASI-derived SO_2 masses and plume heights between the two eruptive periods, with the 2019–2020 eruption having lower overall SO_2 masses and lower maximum plume heights compared to the 2023 eruption (Table 1; Fig. S.1). The cumulative IASI-derived SO_2 mass for the 2023 eruption is 108.1 kt, nearly 7x greater than the cumulative IASI SO_2 mass of 15.7 kt found for the 2019–2020 Shishaldin Volcano eruption. This supports the initial TROPOMI findings that the 2023 eruption released a substantially greater quantity of SO_2 relative to the 2019–2020 eruption.

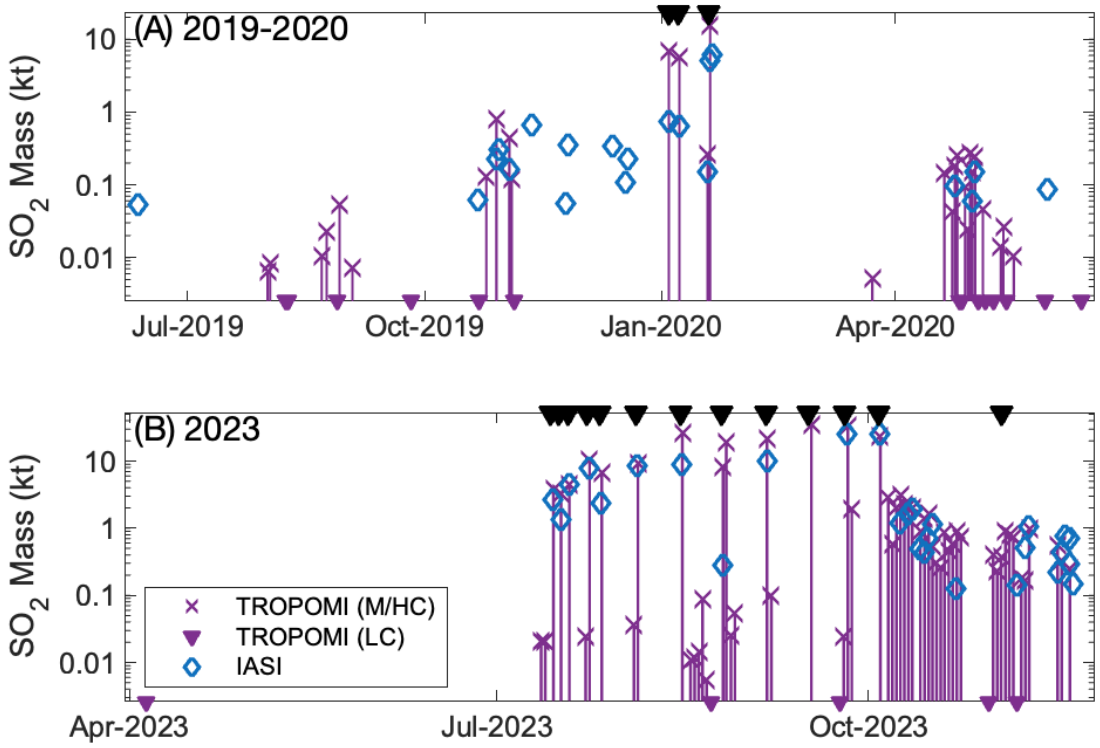


Figure 6: Time series observations of TROPOMI and Infrared Atmospheric Sounding Interferometer (IASI) Shishaldin Volcano SO_2 detections and masses for the (A) 2019–2020 and (B) 2023 eruptive periods. TROPOMI SO_2 masses from medium- (M) and high-confidence (HC) detections are shown as purple bars with 'x' symbols on top and IASI SO_2 masses are shown as blue diamonds. Purple triangles on the lower x-axis mark low-confidence (LC) TROPOMI detections (masses not quantified). Black triangles on the upper x-axis mark explosive events (paroxysms).

3.2 Airborne Gas Compositions

Of the seven airborne gas flights conducted between 2015 and 2024, six yielded SO_2 emission rates, two quantified H_2O, CO_2 and SO_2 compositions, and one quantified CO_2 and SO_2 only (Table 2). The 2015 and 2019 gas flights occurred within eruptive periods, while the others occurred within inter-eruptive quiescence. H_2S was not detected on any of the gas flights, indicating high-temperature gas emissions with minimal impact of hydrothermal scrubbing (e.g., Symonds et al., 2001). SO_2 emission rates ranged from a low of 80 ± 20 t/d seen in 2021 (between the 2019–2020 and 2023 eruptions) and a high of 770 ± 220 t/d in August 2015, during the prior eruption of Shishaldin Volcano in 2014–2015 (Table 2). Low molar CO_2/SO_2 ratios of 2.2 ± 0.4 and 1.4 ± 0.1 were observed during the 2019–2020 eruption and following the 2023 eruption, respectively (Table 2), consistent with a relatively shallow magma degassing source (e.g., Werner et al., 2020). In contrast, on 4 September 2020, approximately six months following the end of the 2019–2020 eruption, a strong volcanic CO_2 anomaly was observed (29 ppm CO_2 and 1.7 ppm SO_2 above background, compared to anomalies of 6 ppm CO_2 and 2.4 ppm SO_2 in 2019). The CO_2/SO_2 ratio in 2020 of 10.8 ± 0.9, combined with the strong CO_2 anomaly, is consistent with a deeper magma degassing source (e.g., Burton et al., 2007; Aiuppa et al., 2007; Werner et al., 2013). Bulk gas compositions were calculated from the September 2020 and August 2024 gas flight data and yielded a fairly consistent gas composition of ~97% H_2O, ~2% CO_2, and ≤1% SO_2 (Table 3). These compositions combined with SO_2 emission rates yield total (post-eruptive) volatile ($H_2O+CO_2+SO_2$) emission rates of ~15,400 t/d and 8,300 t/d for 2020 and 2024 gas flights, respectively (Table 3). Of the four gas flights conducted here that overlap with our TROPOMI time series from 2019–2023, no coincident TROPOMI detections were made to allow direct comparisons between TROPOMI and airborne SO_2 emission rates. This is not surprising since the airborne emission rates during that period were all similar to the TROPOMI detection limit, estimated at ~100–200 t/d (Theys et al., 2019).

Table 2: Molar Airborne Gas Compositions and SO_2 Emission Rates

Date (MM-DD-YYYY)	H_2O/CO_2 ± RMSE	CO_2/SO_2 ± RMSE	*H_2O/SO_2 ± RMSE	SO_2 Emission Rate (t/d) ± Total Uncertainty
08-18-2015	n.d.	n.d.	n.d.	770 ± 220
07-23-2019	n.d.	2.2 ± 0.4	n.d.	170 ± 60
08-16-2020	n.d.	n.d.	n.d.	100 ± 40
09-04-2020	47.2 ± 2.4	10.8 ± 0.9	510.9 ± 47.6	n.m.

07-03-2021	n.d.	n.d	n.d.	80 ± 20
07-30-2024	n.d.	n.d.	n.d.	510 ± 80
08-01-2024	64.0 ± 2.7	1.4 ± 0.1	89.0 ± 4.9	310 ± 70

n.d. indicates at least one species was not detected to allow for ratio calculations, n.m. indicates measurements were not attempted. Root Mean Square Error (RMSE) represents the root mean square error on the measurements. *Calculated from measured ratios.

Table 3: Bulk Gas Composition and Total Volatile Emission Rates

Bulk Gas Composition					
Date	**H_2O mol%**	**CO_2 mol%**	**SO_2 mol%**	**H_2S mol%**	**Total**
09-04-2020	97.74 ± 0.11	2.07 ± 0.10	0.19 ± 0.02	n.d.	100.00
08-01-2024	97.38 ± 0.11	1.52 ± 0.06	1.09 ± 0.06	n.d.	99.99
Emission Rates					
Date	**H_2O t/d**	**CO_2 t/d**	**SO_2 t/d**	**H_2S t/d**	**Total t/d**
*8-16 & 9-4-2020	14,500 ± 6,200	800 ± 320	100 ± 40	n.d.	15,400 ± 6,500
08-01-2024	7,700 ± 1,900	300 ± 70	300 ± 70	n.d.	8,300 ± 2,000

n.d. indicates not measured. Total uncertainties are presented following ±. *In the absence of coincident emission rates and compositions on either day, gas compositions from 4 September 2020 were combined with SO_2 emission rate from 16 August 2020 to calculate total volatile emission rates.

4. Discussion:

4.1 Comparison between IASI and TROPOMI SO_2 Observations

We first compare TROPOMI and IASI SO_2 measurements to evaluate agreement between the detection capabilities and derived masses under different conditions (e.g. seasons, plume altitudes). We conduct a quantitative evaluation of plume SO_2 masses and heights based on coincident detections and a qualitative analysis of time series trends seen in both datasets.

A total of 33 Shishaldin Volcano SO_2 plumes were detected within 3.33 hours of each other by both IASI and TROPOMI sensors over the 2019−2020 and 2023 eruptive

periods. Of these matched detections, 14 (~42%) of them were associated with large SO_2 masses emitted during paroxysmal events (Fig. 6; Table S.1). Both sensors captured most explosive events, with the exception that Events 8 and 10 from the 2023 eruption were only detected by TROPOMI and SO_2 from Event 13 could not be quantified by either sensor due to the presence of a large quantity of SO_2 from Kliuchevksoi Volcano (Kamchatka, Russia) over Alaska airspace during Shishaldin Volcano's Event 13. For the 33 matched detections, we find a strong positive correlation between TROPOMI and IASI derived plume SO_2 masses and plume heights, with Pearson correlation coefficient (r) values of 0.88 and 0.78, respectively (Fig. 7). We also calculate the coefficient of determination (r^2) between these datasets and find variances in SO_2 mass and plume height of 0.78 and 0.61, respectively. For 81% of matched detections, TROPOMI yielded higher SO_2 masses than IASI with a median percent difference between IASI and TROPOMI of -46% (Table S.4). No apparent bias was observed between TROPOMI- and IASI-derived plume heights, with a median percent difference of ~6% (Table S.4). Some discrepancies in event SO_2 mass can be attributed to IASI overpasses occurring several hours prior to TROPOMI overpasses while multi-hour eruptions were underway (e.g., Events 3a (2020) and 8 in Figs. 7, S.2; Table S.1), or the potential bias of taking the average of all three IASI-derived morning SO_2 masses, in the case when not all images have complete plume coverage.

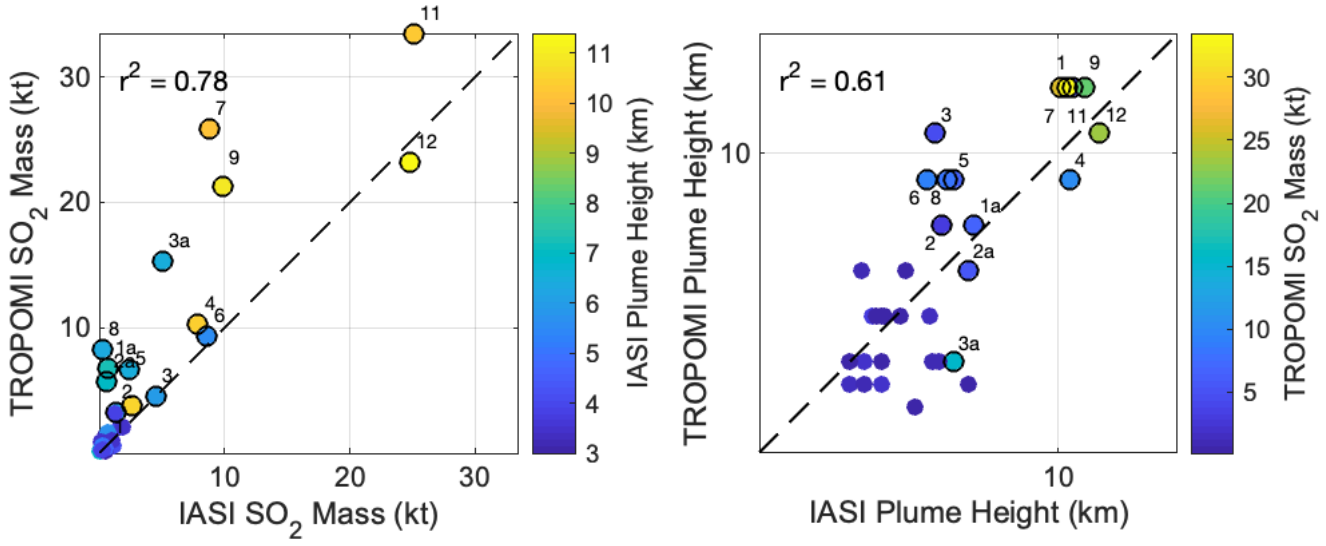


Figure 7: Comparison between coincident IASI and TROPOMI Shishaldin Volcano SO_2 masses (left) and plume heights (right) throughout 2019–2020 and 2023 eruptive episodes. Symbol colors reflect IASI plume height in km (left) and TROPOMI SO_2 mass in kt (right). Dashed black lines indicate a 1:1 agreement. All detections associated with paroxysmal events are labeled, with the 2019–2020 eruption events distinguished as "a".

Time series of SO_2 detections by IASI and TROPOMI show good agreement for spring through fall detections when SO_2 masses exceed 0.1 kt but reveal several missed detections by TROPOMI during the winter (Fig. 6), illustrating its seasonally variable detection limit. A marked difference in detection capabilities by TROPOMI between the 2019–2020 (summer to winter) and 2023 (summer to fall) eruptions is expected, due to the limited wintertime UV radiation at high latitude locations, such as Alaska, which substantially increases the TROPOMI detection limit (e.g., Carn et al., 2013; Lopez et al., 2013; 2020). Throughout the two eruptive episodes, TROPOMI detected numerous plumes in spring through fall with SO_2 masses <0.1 kt, including several with masses <0.01 kt and several low-confidence detections with masses not calculated. In contrast, during the months of November through January, IASI detected several SO_2 plumes with masses approaching or exceeding 0.1 kt that were undetected by TROPOMI. The relatively higher IASI detection limit is likely a function of both its larger pixel size and lower sensitivity to low-altitude plumes, which would hinder detection of smaller and weaker SO_2 plumes more typical of the 2019–2020 eruption. For the 2023 summer eruption, we see very good agreement between daily detection trends and SO_2 masses quantified by both IASI and TROPOMI (Fig. 6).

Unlike TROPOMI, IASI exhibits a fairly stable detection limit based on the large number of Shishaldin Volcano detections with SO_2 masses of ~0.1 kt. Because IASI does not depend on UV radiation, it does not exhibit the seasonal variation in detection limit shown by UV sensors, providing a more consistent dataset at high latitudes. These results imply that while TROPOMI has excellent summer detection capabilities in Alaska, combining TROPOMI and IASI datasets provides a more complete record of volcanic SO_2 degassing throughout the year.

We next compare SO_2 masses measured by TROPOMI and IASI for matched and unmatched detections to further explore each sensor's capabilities and limitations. Our previous analysis found that IASI regularly measured smaller SO_2 masses than TROPOMI for the same detection. To estimate how much SO_2 from Shishaldin Volcano IASI missed for these matched detections we calculate the cumulative SO_2 mass for matched detections by TROPOMI of 168 kt compared to 105 kt measured by IASI (Fig. S3), indicating that IASI underestimated measured SO_2 masses by ~63 kt for the 2019−2020 and 2023 study periods. Next, we consider how much SO_2 IASI missed due to undetected small or weak SO_2 plumes. TROPOMI measured a cumulative SO_2 mass for unmatched detections (only seen by TROPOMI) of 99 kt relative to the IASI's 19 kt SO_2 for unmatched detections, a difference of 80 kt (Fig. S.3). If we sum the masses of SO_2 missed by IASI for both matched and unmatched (TROPOMI only) detections we find that IASI missed ~143 kt of SO_2 from Shishaldin Volcano, with 44% due to underestimating SO_2 from matched detections and 56% due to missed

detections of small, weak and/or low-altitude plumes (Fig. S.3). To estimate how much SO_2 TROPOMI missed due to its higher winter-time detection limit in Alaska, we use the cumulative IASI SO_2 mass for unmatched IASI detections of ~19 kt. Finally, by dividing the amounts of SO_2 missed by IASI (~143 kt) and TROPOMI (~19 kt) out of the total cumulative SO_2 mass of 279 kt, calculated below, we find that IASI and TROPOMI missed ~51% and ~7%, respectively, of the measured SO_2 emissions from Shishaldin Volcano. We note that it is likely that additional plumes that were either small (<100-200 t/d) or masked by clouds went undetected by both satellite sensors, but without continuous measurements by more sensitive airborne or ground-based instruments, the quantity of undetected SO_2 remains unknown.

4.2 Differences in Cumulative and Event SO_2 Masses of Recent Shishaldin Volcano Eruptions

We combine both TROPOMI and IASI datasets to calculate robust cumulative SO_2 masses for both the 2019–2020 and 2023 Shishaldin Volcano eruptions. We first define a best SO_2 mass per day by selecting the available measurement when only one sensor made a detection, and the maximum SO_2 mass calculated on days when both sensors produced matched detections. We then calculate the total Shishaldin Volcano 2019–2020 and 2023 eruption SO_2 masses by summing these daily best estimates. We identified 39 unique daily SO_2 (medium- to high-confidence) detections during the 2019–2020 eruption (11 from IASI, 19 from TROPOMI, and 9 matched detections seen by both sensors) that produced a total eruptive SO_2 mass of 39.6 kt (Fig. S.3). In comparison, for the 2023 eruption, there were 63 unique detections (6 from IASI, 35 from TROPOMI, and 22 matched detections seen by both sensors) with a total cumulative eruptive SO_2 mass of 239.8 kt. The 2023 eruption thus produced six times more SO_2 than the 2019–2020 eruption (results summarized in Figure S.3; details in Tables S.1, S.4). Summing both eruptive episodes yields a total of 279.4 kt of SO_2 produced by Shishaldin Volcano over these two eruptive episodes.

We next compare explosive event SO_2 masses for 2019–2020 and 2023 eruptions against the SO_2 mass calculated for the 19 April 1999 sub Plinian eruption from Carn et al. (2015). The SO_2 masses calculated for the three 2020 explosive events ranged from 5.7–15.3 kt, with Event 3 having a substantially higher mass than the previous two events. The SO_2 masses for the 2023 explosive events ranged from 3.2 to 34.7 kt, with Events 1–6 having relatively lower masses (<10 kt), compared to Events 7–12 whose masses ranged from 19.2–34.7 kt (Table S.1 and Loewen et al., 2026). Shishaldin Volcano's 1999 eruption had two explosive events, on 19 and 23 April. The 19 April event was substantially more explosive and was the only one with quantified SO_2 emissions (Nye et al., 2002; Carn et al., 2015), though satellite detection limits were

much higher at that time. Using data from the Total Ozone Mapping Spectrometer (TOMS) Carn et al. (2015) calculated an SO_2 mass of 63 kt for the 19 April 1999 explosive event. This value is nearly twice the SO_2 mass released during the largest event of 2023 (Event 10, 34 .7 kt), and nearly twice the cumulative SO_2 mass released over the entire 2019–2020 eruption (~40 kt), suggesting that the 1999 event involved substantially more magma than any individual 2023 event or the entire 2019–2020 eruption. Unfortunately, we do not have additional time series constraints on SO_2 emissions from the 1999 eruption to evaluate how the cumulative 1999 SO_2 mass compared with that of the 2023 eruption. These results are broadly consistent with maximum plume height estimates for each of these three eruptions, where the highest SO_2 mass corresponds to the highest 16 km plume height estimated for the 1999 eruption (Nye et al., 2002), slightly lower masses for 2023 explosions, where plume heights reached 14.0 km, and the lowest mass for 2020 paroxysms which only reached 9.8 km altitudes (Loewen et al., 2026b; Gomez-Patron et al., 2026).

4.3 SO_2 Degassing Trends for Forecasting and Tracking Eruptive Activity for the 2019−2020 and 2023 Eruptions

TROPOMI- and IASI-detected SO_2 emissions during the 2019–2020 eruption correspond well with eruption periods at Shishaldin Volcano, but provided minimal advanced warning of the eruption, nor did they capture the eruption onset consisting of spatter cone growth and Strombolian explosions (Fig. 5). The potential exception to this was a single IASI detection made on 11 June 2019, ~1 month prior to the eruption onset. Long-period seismicity and tremor may also have occurred as early as mid-June 2019 (Orr et al., 2023) which suggests that this IASI detection could have been an eruption precursor, though the diffuse nature of the signal suggests it could instead be SO_2 from another source that was simply captured near Shishaldin Volcano. Besides this single potential SO_2 detection seen in June, SO_2 was not detected by either TROPOMI or IASI until August 2019, ~2 weeks following eruption onset, suggesting that early eruptive emission rates were likely low (<100–200 t/d), masked by clouds, or very low in altitude. A cluster of SO_2 detections with emission rates of several hundred tons per day observed in August and September, which may have been due to favorable viewing conditions capturing degassing associated with low-level eruptive activity (Loewen et al., 2026a). No SO_2 emissions were detected during the mid-September to mid-October eruption hiatus. Elevated SO_2 emissions were seen in late October and through mid-December 2019 in TROPOMI and IASI, with TROPOMI derived SO_2 emission rates exceeding 1000 t/d on multiple occasions between 24 October and 3 November 2019, likely associated with more active effusive activity that resulted in repeated lava flows spilling onto the north flank of the edifice (Loewen et al., 2026a). The highest SO_2 emission rates were detected during the January explosive

paroxysmal events, with emission rates exceeding 23,000 t/don 3, 7 and 19 January 2020. A final period of elevated SO_2 emissions was seen from March through May of 2020. During this period, detections were made on almost a daily basis. Many of these spring detections were low confidence, with emission rates of <100 to ~700 t/d SO_2 when calculated. While this period of degassing was primarily after the eruption finished, we expect it represents either degassing of residual magma from the 2019–2020 eruption or degassing of a recharging magma following evacuation of the shallow volcanic system during the eruption.

SO_2 emissions during the 2023 eruption also corresponded with elevated eruptive activity, with detections largely absent prior to the eruption onset, and rarely seen during weakly explosive eruptive activity between paroxysms. In fact, one key observation seen from the five years of Shishaldin Volcano TROPOMI time series is that SO_2 was rarely detected by satellite outside of periods of unrest or eruption (e.g., as characterized by AVO's elevated Aviation Color Code; Gardner and Guffanti, 2006; Fig. 5). The one exception was the single low confidence detection seen in April 2023 (Fig. 2a) following a brief period of seismic tremor and approximately three months prior to the 2023 eruption onset. No other detectable degassing was identified prior to the 2023 eruption onset in either TROPOMI or IASI data, but elevated emissions of ~500 and nearly 700 t/d SO_2 were derived from TROPOMI data on 11 and 12 July, corresponding with the eruption onset. Then very distinct patterns of elevated gas emissions were seen corresponding with explosive Events 1 through 12 (from mid-July through October) in TROPOMI and IASI datasets. Specifically, SO_2 emission rates approaching or exceeding 10,000 t/d immediately followed each explosive event, with minimal SO_2 detections seen between events. Notably, Events 4, 6 and 11 showed detectable degassing of a few 100 t/d of SO_2 in TROPOMI imagery in the hours preceding paroxysmal events following days without detectable SO_2 emissions (Figs. 5, 6, 8). We interpret this to represent degassing during vigorous Strombolian eruptions that often preceded the paroxysmal events (Fee et al., 2026) combined with fortuitous satellite overpass timing. This suggests that increases in SO_2 emissions likely precede Shishaldin Volcano paroxysmal events by several hours, and that if acquired at a sufficient temporal resolution, SO_2 emission rates could help forecast these explosive paroxysmal events.

Following Event 12 (early October), the degassing behavior changed from discrete periods of elevated SO_2 emissions seen almost exclusively associated with explosive paroxysms to persistently elevated SO_2 emissions (~1000 t/d) seen on a near-daily basis, without an obvious increase in eruptive activity. This dramatic change in SO_2 emission style also corresponded with an increase in elevated surface temperatures (Loewen et al., 2026a) and was initially interpreted as a change in eruption style from

explosive to effusive. However, once clear satellite imagery was available, it confirmed that lava had not erupted at the surface. Therefore, we interpret this phase of the eruption to reflect degassing of a shallowly emplaced magma, either convecting or slowly ascending within the conduit itself, or intruded into the shallow edifice. Further analysis by Angarita et al. (2026a) suggests that the formation of a summit crater crack on 28 August (Fig. 4) and its expansion on 3 October 2023 may have been due to shallow dike emplacement. The timing of the expansion of this crack feature and dike emplacement in early October is consistent with our persistently elevated SO_2 emissions and interpretation of shallow magma degassing. The eruption of Kliuchevskoi Volcano prevented calculations of Shishaldin Volcano SO_2 masses and/or emission rates by either TROPOMI or IASI for Event 13, though persistent SO_2 emissions were detected prior to and following this event (Table S.1; Fig. 8).

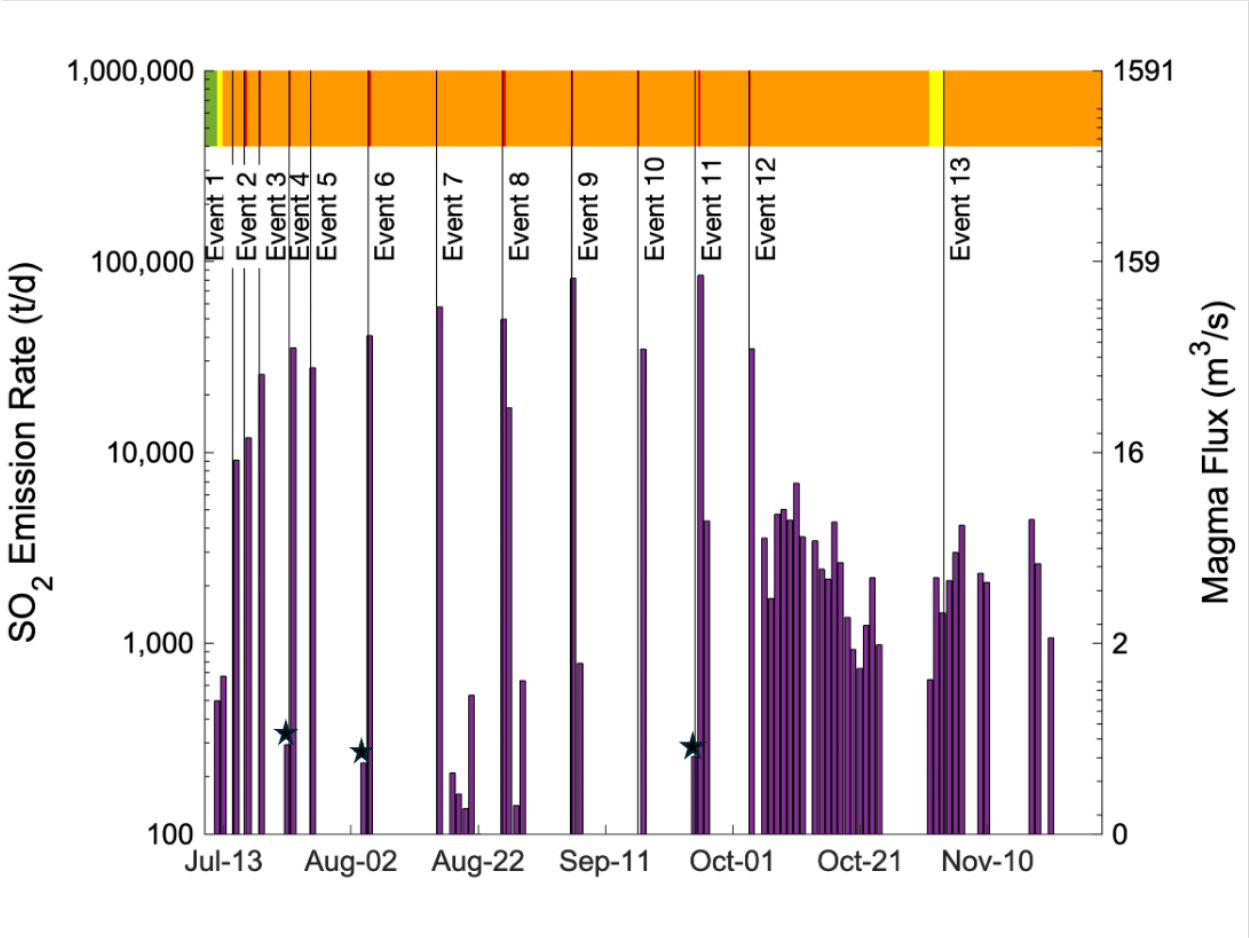


Figure 8: TROPOMI derived SO_2 emission rates (purple bars, left axis) and calculated magma fluxes (right axis) for the 2023 eruption and plotted on a log scale. Shishaldin Volcano's Aviation Color Code (Gardner and Guffanti, 2006) is plotted at the top as a proxy of volcanic activity. Each explosive event is marked by a vertical black line. Black stars indicate pre-paroxysmal degassing. Note that emissions from Event 13 could not

be quantified due to the presence of a large SO_2 plume from Kliuchevskoi Volcano over Shishaldin at that time.

4.4 Insights into Gas Exsolution and Separation from Degassing Models

SO_2 emissions are commonly used to track magma supply into the shallow crust (e.g., Aiuppa et al., 2023). If exsolved SO_2 can separate from its host magma (open-system degassing) and find a permeable path to Earth's surface, SO_2 will be released by a volcano before the magma reaches the surface (e.g., Shinohara et al., 2008). Because the depth of SO_2 exsolution and degassing can be quite shallow for low-H_2O (e.g., <2 wt.%) basaltic systems, SO_2 may provide little advance warning of ascending magmas (e.g., Gerlach, 1986; Lerner et al., 2021). SO_2 exsolution depth can vary substantially across different magmatic systems depending on melt composition, temperature, oxygen fugacity (fO_2), and sulfur speciation (e.g., S^{2-} vs S^{6+}), such that modeling SO_2 degassing requires volcano-specific petrologic constraints (Edmonds and Wallace, 2017). Here, we use petrologically-constrained thermodynamic and empirical H-C-S degassing models of Shishaldin Volcano magma to help interpret our satellite and airborne gas data. We assume a basaltic melt composition based on a primitive melt inclusion from the 1999 eruption (sample SH63MI41, 46.5 wt.% SiO_2, 5.3 wt.% MgO; Rasmussen et al. 2018) and use the best available melt inclusion constraints on volatiles from the 1999 and 2023 eruptions from Rasmussen et al., (2018) and Izbekov et al. (2027), respectively, assuming that similar magma sources and compositions persist among recent eruptions. For initial volatile concentrations we use a maximum melt S concentration of ~1700 ppm S from the 2023 eruption determined from Izbekov et al. (2027, Table S.5). Because H_2O and CO_2 concentrations have not been analyzed in melt inclusions for the 2023 eruption at the time of this writing, we assume initial H_2O and CO_2 concentrations based on maximum melt inclusion volatile concentrations of 2.5 wt.% H_2O and ~2600 ppm CO_2 from the 1999 eruption (Rasmussen et al., 2018).

We apply the Sulfur_X thermodynamic degassing model (Ding et al., 2023), which models the degassing of CO_2, H_2O, and S species. The Sulfur_X calculations simulate both open- and closed-system degassing (Figs. 9, 10), using the H_2O-CO_2 degassing model of Iacono-Marziano et al. (2012). We assume a melt temperature of 1120°C and an oxygen fugacity of +0.9 log units relative to the fayalite-magnetite-quartz buffer (ΔFMQ +0.9) to simulate initial S^{6+}/S^{total} ratios of 0.3–0.4 (pressure-dependent), to match the range of measured S^{6+}/S^{total} ratios determined from S k-alpha peak positions (described in Supplementary Materials A, B and Table S.5 using data from Izbekov et al., 2027). The sulfur speciation, which is a key parameter in modeling sulfur behavior, is calculated from fO_2 via the model of O'Neill and Mavrogenes (2022), as implemented within Sulfur_X. Melt oxygen fugacity was kept fixed during the model runs (i.e., magma-buffered fO_2). Isothermal models were run with a range of initial CO_2 concentrations in order to simulate the ascent of magma starting from different depths of 850, 2000, and 2600 ppm CO_2,

corresponding to starting volatile saturation depths of ~6, 10, and 12 km below the surface, consistent with a geodetically modeled deep magma source (Angarita et al., 2026a). A complete list of model inputs can be found in Table S.6. Both open- and closed-system degassing modeling were performed to put bounds on the range of possible exsolving gas compositions. The Sulfur_X degassing models are in reasonable agreement with petrologic measurements of volatiles in melt inclusions from Shishaldin Volcano's 1999 eruption (Rasmussen et al., 2018), providing confidence in the model results (Fig. S.5).

Sulfur_X closed- and open-system degassing model results indicate that CO_2 is initially the dominant volatile exsolving from the melt during ascent from mid-crustal depths, with H_2O and S remaining mostly dissolved until magma reaches depths less than ~2–4 km below the surface (Figs. 9a, 10a; Tables S.7-S.12). Differences in open- and closed-system degassing styles are quite minimal for Shishaldin Volcano melts (Figs. 9, 10), with the main difference being whether initially exsolved CO_2 remains within the melt and buffers further volatile exsolution (closed-system) or is fully lost from the magma (open-system). In open-system degassing, CO_2 is more thoroughly degassed during deep ascent, with almost all the CO_2 lost from the melt by ~3 km depth (compared to ~2 km in closed-system degassing). Sulfur and H_2O start degassing extensively and abruptly at depths of 2–3 km in open-system degassing, and slightly deeper and more gradually in closed-system degassing (2–4 km), with H_2O being the dominant degassing species at shallower depths within the conduit.

In both closed- and open-system degassing styles, the total extent of volatile exsolution is relatively low until magma ascends to very shallow depths, with approximately half of the initially dissolved volatiles exsolving into a separate fluid phase at a depth of ~1 km (Figs. 9b, 10b). The remaining 50% of total volatiles exsolve from the melt in the final ~1 km of ascent to the surface. Consequently, emission rates of SO_2 (and H_2O) would be relatively low until the Shishaldin Volcano magma ascends to near-surface depths (e.g., <1–2 km below the surface).

We additionally apply an empirical degassing model based on fits to petrologic measurements of H_2O, CO_2, and S in melt inclusions from Shishaldin Volcano's 1999 eruption (Rasmussen et al., 2018), following an approach described in Werner et al. (2020). The empirical fit to the 1999 melt inclusion data are generally consistent with the Sulfur_X modeling (acknowledging variability in the underlying melt inclusion values; Fig. S.4), indicating that CO_2 is the main degassing volatile until depths of <4 km, with sulfur and water beginning to substantially exsolve from the melt with further ascent (Fig. S.5).

The model results enable comparison of anticipated ratios of exsolved gases (CO_2/SO_2, H_2O/CO_2) with measured volcanic gas compositions from gas flights (Figs. 9c, 10c). The low CO_2/SO_2 ratios measured in 2019 and 2024 are consistent with Sulfur_X-modeled gases exsolved from magma at depths of 3.5−4 km (open-system) or 2−4 km (closed-system) across the range of initial melt CO_2 concentrations. In contrast, the higher CO_2/SO_2 ratio of ~11 measured in 2020 can best be explained by a deeper magma source at ≥12 km for both open- and closed-system degassing models. Airborne-measured H_2O/CO_2 ratios of ~47−64 can be reproduced from Sulfur_X models at shallow depths (<1 km) from closed-system degassing of the melt with the lowest initial CO_2 composition (850 ppm, Fig. 9c), or by open-system degassing of a melt of any initial CO_2 composition at depths of ~2.5−3 km (Fig. 10c). Since these H_2O/CO_2 ratios were observed during quiescence in 2021 and 2024 following eruptions without corresponding persistent, elevated surface temperatures that may be expected for magma at depths < 1 km, we prefer the open-system degassing model. The slight (0.5-1.5 km) differences in open-system magma degassing depths inferred from the two measured gas ratios (~3.5-4 km for CO_2/SO_2 vs. ~2.5-3 km for H_2O/CO_2) can be explained by uncertainties in our degassing model assumptions and/or the occurrence of depth-integrated degassing of a column of magma within this depth range (e.g., Edmonds et al., 2022). Additionally, because Shishaldin Volcano is a snow- and ice-covered volcano, there is also the potential for external water to be added to the gas plume. This would increase the H_2O/CO_2 ratio of gas compared to expectations from petrologic models, such that actual magma degassing depths would be deeper than the magmatic degassing model estimates.

These combined results indicate that Shishaldin Volcano melt was primarily degassing at depths of <2−4 km below the summit (near sea level) during and following eruptions when low CO_2/SO_2 (<2.2) and high H_2O/CO_2 (47−64) ratios were observed (Table 2; Figs. 9, 10). The high CO_2/SO_2 gas ratio and CO_2 emission rate measured in-between eruptions in 2020 reflects degassing from magma at depths of >12 km, which we hypothesize represents the process of deep magma recharge between eruptions. This high measured CO_2/SO_2, combined with periods of elevated SO_2 emissions between eruptive events (e.g., Events 12-13, Fig. 8), and the assumed low-viscosity basaltic magma (see Supplementary Material B) all support gas-melt separation and suggest that open-system degassing is the dominant behavior at Shishaldin Volcano - at least during quiescence. We propose that exceptions to this behavior occur during explosive eruptions, when fast magma ascent impede gas separation from the host melt, leading to closed-system degassing during paroxysmal events (Parfitt & Wilson, 1995).

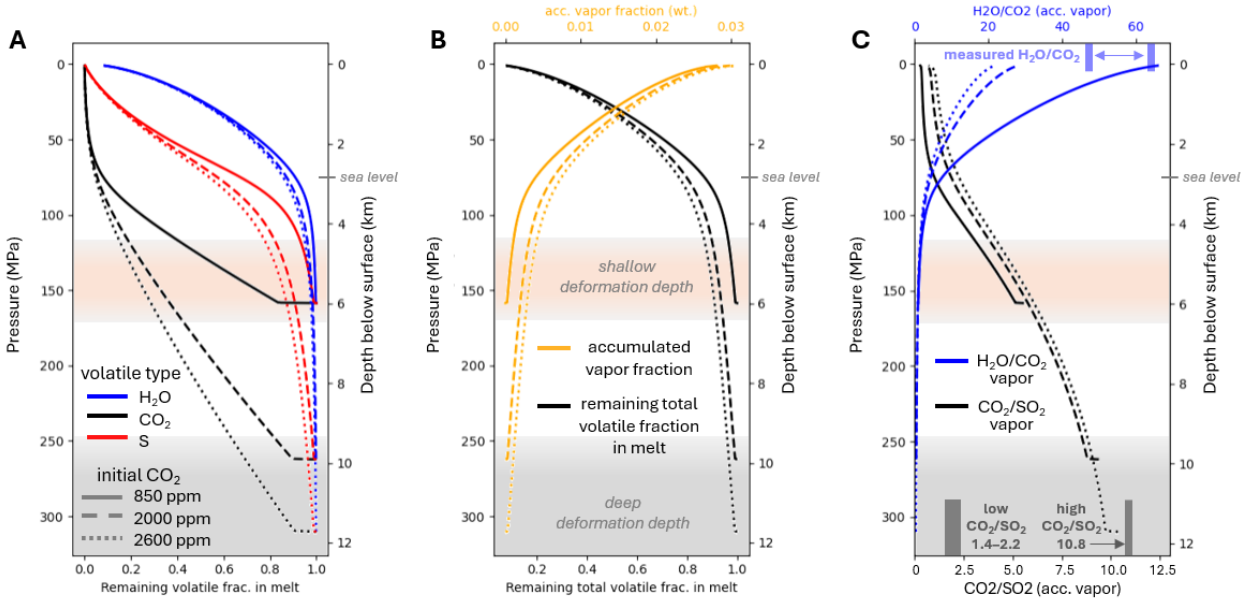


Figure 9: Sulfur_X closed-system isothermal degassing model for a Shishaldin Volcano basaltic melt (assuming 1120°C, fO_2 = ΔFQM+0.9, S^{6+}/S^{total} 0.3−0.4) using the CO_2-H_2O degassing model of Iacono-Marziano et al. (2012). The modeled melt initially contains 1710 ppm S and 2.5 wt% H_2O, and three different initial CO_2 concentrations are modeled: 850, 2000, and 2600 ppm (respectively solid, long dashed, and dotted lines across all panels). *A)* Fraction of S (red), CO_2 (black) and H_2O (blue) remaining dissolved in the melt as magma ascends. *B)* Total volatile mass fraction remaining in the melt (black) and partitioned into an accumulated exsolved volatile phase (yellow). *C)* H_2O/CO_2 (blue) and CO_2/SO_2 (black) compositions of the accumulated exsolved vapor phase, with airborne-measured CO_2/SO_2 and H_2O/CO_2 gas compositions shown as bars along the bottom and top axes (see Table 2). Depth below the surface assumes a crustal rock density of 2700 kg/m^3. Horizontal shaded regions indicate the approximate depth of the Shishaldin Volcano deformation sources (possible magma reservoirs) from Angarita et al. (2026a). See text for further details.

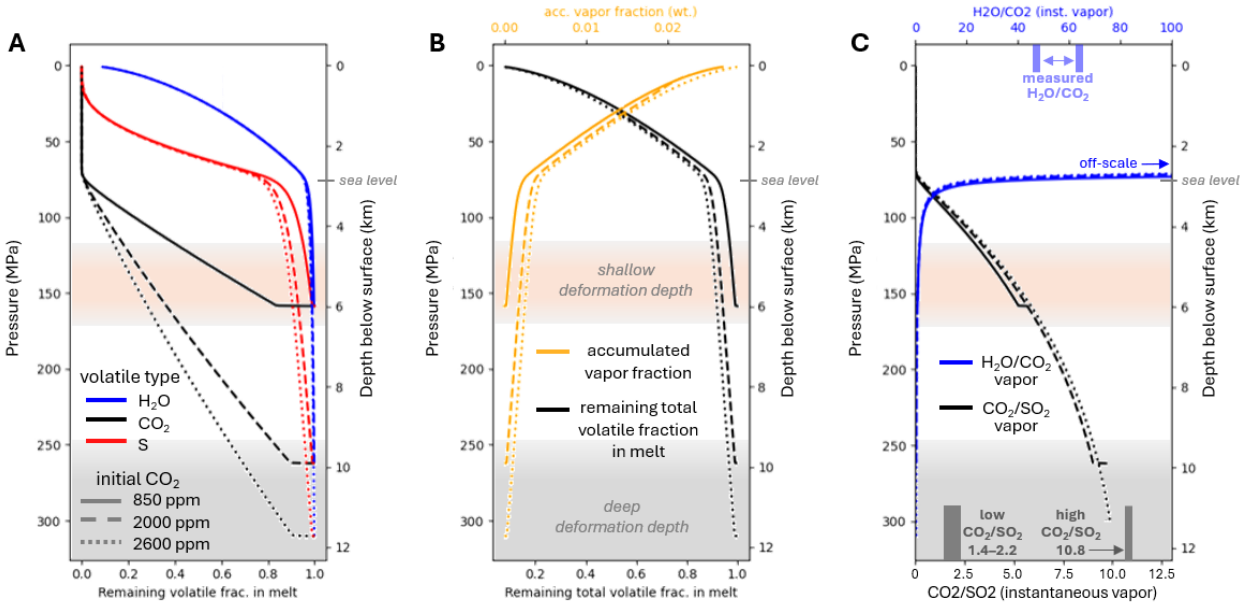


Figure 10: Sulfur_X open-system isothermal degassing model for a Shishaldin Volcano basaltic melt. Model conditions and figure symbology are the same as in Fig. 9. Panel C shows CO_2/SO_2 and H_2O/CO_2 ratios of gas released instantaneously during each pressure-step of open-system degassing (total accumulated gas ratios are shown in Fig. S.6). Note that for pressures less than 70 MPa, modeled instantaneously exsolved H_2O/CO_2 ratios substantially exceed 100 and are not plotted here to improve readability. Airborne-measured gas compositions shown as bars along the bottom and top axes (see Table 2).

4.5 Calculations of Degassed Magma Masses and Volumes

The amount of magma that has degassed over an eruptive or unrest period can be calculated from cumulative volcanic SO_2 emissions combined with how much S has been lost from the melt based on melt inclusion analyses, in what is commonly referred to as the petrologic method (e.g., Devine et al., 1984; Gerlach et al., 1994). Because S exsolves from basaltic melts at relatively shallow depths (e.g. Figs. 9, 10), degassed magma masses often agree quite well with eruptive masses for basaltic systems, especially during effusive eruptions (e.g., Sutton et al., 2003; Lerner et al., 2021; Pfeffer et al., 2024). Studies of explosive basaltic eruptions are less abundant, and also find that the majority of magma supplied to and degassed within the shallow system erupted (e.g., Aiuppa et al., 2021; Coppola et al., 2019). Consequently, we calculate degassed magma masses and use these to estimate eruption masses during our study period. We acknowledge that this method may overestimate total eruption masses as not all magma that degasses erupts, and it is common for open-vent volcanoes, such as Shishaldin Volcano, to degas more magma than they erupt, especially over extended time periods (e.g., Shinohara, 2008; Edmonds et al., 2022). However, because limited SO_2 was detected between eruptions we consider non-eruptive degassing during the

study period to be minor. Furthermore, we expect the total satellite-derived SO_2 masses used in this calculation to be underestimated due to limited detection capabilities during cloudy and/or wintertime conditions, which would partially offset any potential overestimation of eruption mass.

Here, we combine cumulative SO_2 emission masses from satellite data over Shishaldin's 2019–2020 and 2023 eruptive periods with petrologic constraints on melt S from the 2023 eruption from Izbekov et al. (2026; Table S.5) to calculate degassed magma masses (M_m) and volumes (V_m). We use a simplified version of the equation from Gerlach et al. (1994),

$$M_{magma} = \frac{E_{SO2}}{2\Delta S \varphi_m} \qquad \text{(eq. 1)}$$

where E_{SO2} is total measured SO_2 gas mass, the factor of 2 in the denominator accounts for the molar mass difference between SO_2 (64 g/mol) and S (32 g/mol), ΔS is the amount of S lost from melt inclusions (representing the deeply trapped, undegassed melt) and the matrix glass (representing the erupted, degassed melt) in mass fraction, and φ_m is the melt mass fraction (i.e., 1 minus the phenocryst fraction). To solve this equation, we use the cumulative satellite-derived SO_2 masses of ~40 kt for the 2019–2020 and ~240 kt for the 2023 eruptive periods and assume an uncertainty of ± 30%. We use data from the most primitive melt inclusion analyzed for the 2023 eruption of Shishaldin Volcano (48.2 wt% SiO_2) from Izbekov et al., (2026; sample 23ESB8a) and assume this composition is representative for undegassed magma of both the 2019–2020 and 2023 eruptions. Specifically, we use an undegassed melt S concentration of 1710 ± 225 ppm, the maximum measured of 29 melt inclusions analyzed by Izbekov et al. (2027; Table S.5). We estimate the residual S in the degassed melt to be 100 ± 50 ppm, which is the maximum S measured in matrix glasses for the 1999 eruption by Rasmussen et al. (2018), and represents eruptive degassing of ~91–97% of S from the initial melt. We use the average groundmass volume fraction measured in four 2023 pumice samples analyzed by Izbekov et al. (2027) of 0.837 ± 0.026 as our estimate for melt fraction and assume negligible difference in converting from volume to mass-based units. Solving equation 1 using the average values above, we calculate total degassed magma masses of 1.5 x 10^{10} kg for the 2019–2020 eruption and 9.0 x 10^{10} kg for the 2023 eruption. To convert degassed magma mass to volume, M_m is divided by melt density (ρ_m). Because we are interested in estimating the degassed magma volume as a proxy for surficial eruption volume, we use a typical dense rock equivalent basaltic

density of 2900 ± 100 kg/m^3 for ρ_m. This yields a degassed magma volume of 5.15 x 10^6 m^3 for 2019–2020 and 30.9 x 10^6 m^3 for the 2023 eruption.

Since our measurements and assumptions all contain uncertainties and many variables have non-normal distributions, we apply a Monte Carlo approach to calculate the most probable results with realistic uncertainties. We conducted 10,000 simulations and used a fixed random seed to ensure reproducibility. We used the mean and standard deviation values provided above, along with (a) log-normal distributions for both the SO_2 and ΔS to maintain positive values, and (b) truncated distributions ranges for melt fraction (0.01–0.99) and melt density (2500–3300 kg/m^3) to be physically realistic. For Shishaldin's 2019–2020 eruption we calculate a median cumulative degassed magma mass of 1.42 x 10^{10} kg (with 90% confidence bounds from 8.3 x 10^9 to 2.5 x 10^{10} kg and listed parenthetically in the following), and a median cumulative degassed magma volume of 4.9 x 10^6 m^3 (2.9 x 10^6 to 8.5 x 10^6 m^3; Fig. 11a). We calculate substantially larger cumulative degassed magma mass and volume for the 2023 eruption, with a median degassed magma masses of 8.6 x 10^{10} kg (5.0 x 10^{10} to 14.8 x 10^{10} kg), and a median degassed magma volume of 29.7 x 10^6 m^3 (17.3 x 10^6 to 51.2 x 10^6 m^3; Fig. 11b). These results further indicate that the 2023 Shishaldin Volcano eruption involved substantially more magma than the 2019–2020 eruption (Fig. S.4). This finding however depends on the assumption of a similar magma supplying both 2019-2020 and 2023 eruptions. Due to the substantial differences in eruption style between these two eruptions, it is possible that the 2019–2020 eruption involved a greater quantity of degassed magma, potentially residual from the 2014–2015 eruption, which led to effusive activity and an overall lower degassed magma volume.

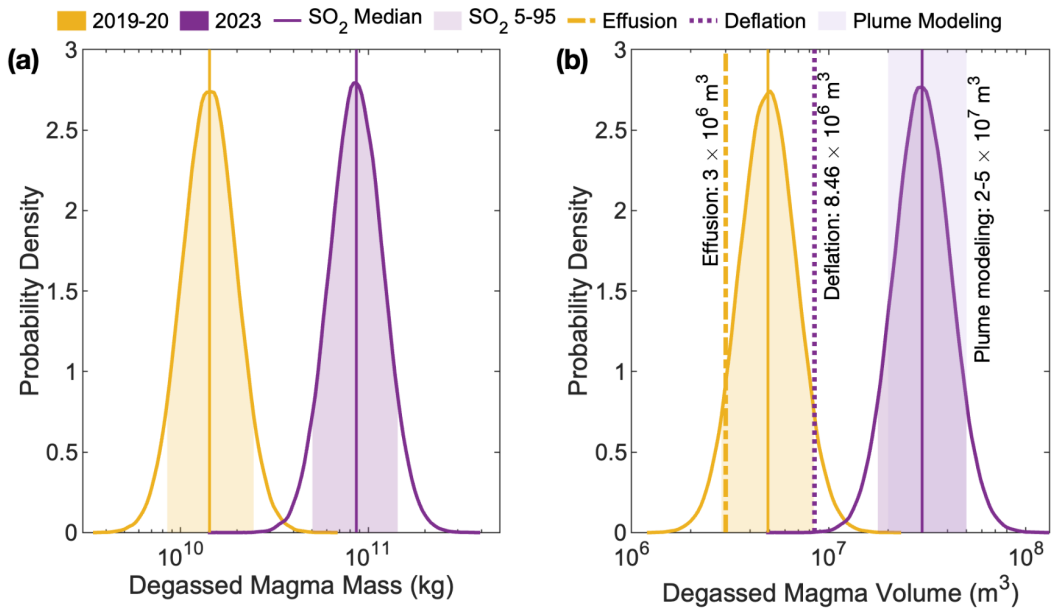


Figure 11: Results from the Monte Carlo simulation of cumulative degassed magma masses (a) and volumes (b) for 2019–2020 (yellow) and 2023 (purple) eruptions of Shishaldin Volcano. Median values are presented as vertical solid lines while 5–95th percentile regions are shown as shaded regions. Degassed magma volumes are plotted in comparison to the 2019–2020 effusive volume (dot-dashed yellow line, Angarita et al., 2026a), the modeled 2023 syn-eruptive deflation volume (dotted purple line; Angarita et al., 2026a) and plume-modeling derived eruption volume (light purple shaded region; Mota et al., 2026).

4.6 Comparison of Eruption Volumes Across Disciplines

We next compare our median degassed magma volumes with prior constraints on eruption size from geophysical and thermal data. No deflation was observed for the 2019–2020 eruption so no geodetic estimate of eruption volume is available (Angarita et al., 2026a). Because the 2019–2020 eruption was largely effusive, Angarita et al. (2026a) calculated an effusive eruptive volume of 3 x 10^6 m^3 based on the radiative power produced by these lava flows as seen in thermal infrared satellite data following previous methods (Saunders-Shultz et al., 2024; Coppola et al., 2017; Harris et al., 1998). Our degassed magma volume calculated for the 2019–2020 eruption of 4.17 x 10^6 m^3 is ~40% larger than the calculated effusive volume (Fig. 11b). The radiative power method is not applicable for explosive events, of which there were three during the 2019–2020 eruption. These explosive events accounted for the majority (~70%) of SO_2 released for the entire eruptive period (27.8 kt vs 39.6 kt; Table S.1). This suggests that effusive lava volume calculated by Angarita et al. (2026a) is a lower bound of the total eruptive volume. If we further assume that some magma degassed but did not

erupt (as supported by the elevated emissions observed in spring of 2020), then the calculated degassed magma masses may overestimate the eruptive volume. Based on our satellite observations (Table S.1) we find that only ~1.6 kt of SO_2 was released from Shishaldin Volcano following the 2019–2020 eruption, <4% of the total. This, in combination with the shallow S exsolution depth found in the degassing models (Figs. 9, 10), suggests that most of the degassed magma likely erupted, and that the degassed magma volume of 4.92 x10^6 m^3 provides a reasonable estimate of the total 2019–2020 eruption volume.

For the 2023 eruption, the co-eruptive deflation volume was modeled as 8.46 x 10^6 m^3 (Fig. 11; Angarita et al., 2026a). Because deflation volume calculations do not account for magma and reservoir compressibility (Kilbride et al., 2016; Angarita et al., 2026b) and may be masked by post-eruptive magma recharge, we consider this volume to be a lower estimate of eruptive volume. Because this eruption was entirely explosive, the radiative power method cannot be applied to estimate eruption volume. As with the 2019–2020 eruption, Shishaldin Volcano continued to degas following the cessation of the 2023 eruption in mid-November. Based on our satellite observations, ~7 kt SO_2 out of a total of ~240 kt SO_2 (<3%) was released in the 1.5 months following eruptive activity. This suggests that most of the degassed magma erupted, and that our median degassed magma volume of 29.7 x 10^6 m^3 represents a reasonable estimate of the 2023 eruption volume. For the 2023 eruption there are also estimates of eruptive volume based on modeling methods to estimate mass eruption rates from plume heights. Mota et al. (2026) use models from Mastin et al. (2014) and Aubry et al. (2023) to calculate a range in the total volume of magma erupted of 20 to 50 x 10^6 m^3. This eruptive volume range agrees exceptionally well with the 5-95 percentile confidence bounds on our degassed magma volume of 17.3 to 51.2 x 10^6 m^3, further indicating that our degassed magma mass is providing a reasonable estimate of the total eruptive volume (Fig. 11).

4.7 Insights into Magma Supply Rates and Eruptive Mechanisms

Collectively, the time series SO_2 observations and degassing models indicate that SO_2 exsolves and likely degasses at relatively shallow depths of <2–4 km below the surface of Shishaldin Volcano. This means that satellite SO_2 emissions at Shishaldin Volcano can track magma ascent within the shallow crust and syn-eruptive emissions, but not the deeper ascent of magma that occurs with limited S degassing. Furthermore, if magma ascends from ~2 km to the surface in less than a day (the approximate TROPOMI repeat cycle), which is likely based on typical magma ascent rates for explosive eruptions (Rutherford, 2008), this potential for detecting a precursory signal will be further reduced. The low SO_2 emission rates measured by gas flights coupled with the lack of persistent satellite SO_2 observations from Shishaldin Volcano between

the 2019–2020 and 2023 eruptions and between the 2023 paroxysms (except for between events 12 and 13) suggests that any magma in the shallow conduit between major eruptions was relatively small in volume and/or already degassed.

The detection of relatively low-level SO_2 emission rates and high CO_2 concentrations between eruptions during gas flights and occasional satellite detections of SO_2 emissions demonstrate that open-system degassing can occur at Shishaldin Volcano months after an eruption (e.g. Table 2). Therefore, it is unlikely that changes in conduit permeability are the main source of the variable gas emissions observed throughout both eruptions (e.g., Fischer et al., 2002; Gaunt et al., 2020). Instead, the four orders of magnitude variability in SO_2 emission rates likely stem from a highly variable magma supply rate to the shallow crust. This behavior is analogous to that of Mount Etna, where Aiuppa and colleagues (2023) found that prior to Mount Etna's 2020–21 paroxysmal events, the magma flux into the shallow crust more than doubled from ~1–3 m^3/s during the precursory phase to nearly ~4–7 m^3/s during paroxysms. This observation supported previous model results that attributed Mount Etna paroxysms to an increasing supply of volatiles to the shallow plumbing system (Aiuppa et al., 2023; Allard et al., 2005). We can calculate Shishaldin Volcano's magma flux following the methods of Aiuppa et al. (2023). In the case of Shishaldin Volcano, we expect S degassing to occur predominantly in the top ~2–4 km of the conduit based on the degassing models. We calculate magma flux to this depth region (Q_{in}) using a modified version of equation 1, that uses SO_2 emission rates (Φ_{SO2}) from our TROPOMI time series dataset, instead of SO_2 mass (Aiuppa et al., 2023):

$$Q_{in} = \frac{\phi_{SO2}}{2\Delta S \varphi_m \rho_m 86.4} \qquad \text{(eq. 2)}$$

where all other variables are the same except we use a lower melt density (ρ_m) value of 2700 kg/m^3 to better represent the pre-eruptive, undegassed melt density. The denominator factor 86.4 converts the SO_2 flux from t/d to kg/s. We assume that melt density remains constant throughout ascent. We calculate magma fluxes ranging from 0.04 to 11 m^3/s (median = 1 m^3/s) for non-eruptive degassing between paroxysmal events, and from 14 to 135 m^3/s (median = 50 m^3/s) during paroxysmal events. This distinct break in magma fluxes between non-paroxysmal and paroxysmal activity further indicates that Shishaldin Volcano paroxysms are driven by relatively high magma fluxes, exceeding 11–14 m^3/s. Because the magma flux calculation scales proportionally to the SO_2 emission rate, the time series trend between these two parameters is identical (Fig. 8). The range in magma fluxes calculated here for Shishaldin Volcano between paroxysms is similar to the range found for Mount Etna

including during and between eruptive paroxysms (Aiuppa et al., 2023). Our order of magnitude higher maximum magma fluxes calculated for Shishaldin Volcano paroxysms relative to Mount Etna can be explained by a lower initial melt S concentration (1710 ppm vs. 2000-3000 ppm) and higher paroxysmal SO_2 emission rates (reaching ~85,000 t/d vs ≤20,000 t/d)), such that much higher magma fluxes are required for the lower-sulfur Shishaldin magmas to generate the higher paroxysmal SO_2 emission rates.

Lastly, we integrate our volcanic gas observations into the context of existing eruption models for Shishaldin Volcano. Angarita et al. (2026a) use deformation data to infer a plumbing system for Shishaldin Volcano that includes a conduit connecting the surface to a pressurized source located ~5–7 km below summit level (~2–4 km below sea level), interpreted to be a shallow magma reservoir. This shallow storage region is connected via a long conduit to a deeper magma source at depths >13 km below the summit (>10 km below sea level). Based on our gas modeling results, CO_2 would be the main volatile exsolving at depths of that deeper magma source, while SO_2 and H_2O begin to substantially exsolve at depths near the top of the shallow reservoir (Figs. 9, 10). Deep recharge may be an initial trigger for Shishaldin Volcano eruptive periods, but the repeating paroxysms during the 2023 eruption suggest that individual explosive eruption timing is modulated by shallower processes, likely within the shallow reservoir or upper conduit.

While several models exist to explain explosive basaltic volcanism, our preferred model for Shishaldin Volcano's 2023 eruption based on gas observations is the rise speed dependent model (Wilson and Head, 1981; Parfitt and Wilson,1995), where eruption style is controlled by magma ascent rate. During high magma ascent rates, gases are unable to separate in advance of their source magma and remain trapped in a homogenous two-phase flow (closed-system degassing behavior), such that gas and magma erupt together explosively (Parfitt, 2004). In this scenario we envision magma rapidly ascending from the top of the shallow reservoir and through the conduit, where substantial volatile exsolution occurs. The repeating nature of Shishaldin Volcano paroxysms (every ~2–10 days for Events 1–12, Fee et al., 2026) could be controlled by the time necessary to refill the shallow reservoir from a deeper magma source following magma evacuation and reservoir depressurization from the previous paroxysm. The assumed high magma fluxes driving paroxysms is consistent with the high SO_2 emission rates observed for 2023 paroxysmal events. This can also explain our observations that indicate Shishaldin Volcano undergoes open-system degassing during quiescence and transitions to closed-system degassing behavior during paroxysms.

An alternative model to explain the repeating paroxysms in basaltic systems is the foam collapse model introduced by Jaupart and Vergniolle (1989), where gases accumulate as a foam at a structural boundary, assumed here to be the top of a shallow magma reservoir, and then collapses to trigger highly explosive basaltic lava fountaining. Vergniolle (2024) expanded on this model and used laboratory experiments to constrain the trigger for the 1999 Shishaldin Volcano paroxysmal eruption. In this model, a very high gas flux combined with very small bubble diameters are required to explain the transition from a stable to unstable foam to ultimately trigger Shishaldin Volcano's 1999 paroxysm (Vergniolle, 2024). Vergniolle attributes these specific parameters to a very large magma ascent rate relative to Mount Etna (and other basaltic volcanoes), consistent with the high magma fluxes calculated for Shishaldin Volcano above. This model is the preferred model invoked for Shishaldin Volcano's 2023 eruption based on seismic and acoustic data (Fee et al., 2026) due to the highly regular timing of the paroxysmal events. Because geodetic observations place the shallow magma reservoir at about ~5 km below the summit (Angarita et al., 2026a), a depth greater than where our models show substantial H_2O exsolution begins (Figs. 9, 10), we prefer the rise speed dependent model, which does not require substantial volatile exsolution to occur beneath a structural boundary.

Decreases in conduit permeability due to magma crystallization and the resulting increase in magma viscosity can also trigger explosive basaltic eruptions (e.g., Di Genova et al., 2020). Based on the observed high inter-eruptive CO_2 emissions that support open-system degassing (Table 2) and the relatively low magma viscosity of ~126–209 Pa·s calculated from petrologic constraints (see Supplementary Materials B), we consider conduit sealing to be a less likely eruption trigger compared to the other models. Future petrologic analyses of Shishaldin Volcano eruption samples and synthesis of multidisciplinary data could provide further insights into the mechanisms controlling Shishaldin Volcano paroxysms.

4.8 Future Work

A key finding of this work is that satellite detectable SO_2 emissions were rarely seen during volcanic quiescence at Shishaldin Volcano during our study period. This suggests that satellite-detectable SO_2 emissions (i.e., rates of 100s t/d) can indicate Shishaldin Volcano unrest and prompt heightened monitoring. We note that elevated SO_2 emissions at Shishaldin Volcano have been observed since 2025 along with elevated seismicity and infrasound, without an eruption. Collectively, these observations, along with our degassing model results, indicate that SO_2 emissions at Shishaldin Volcano likely reflect degassing of shallow magma and may be a key eruption precursor. We observed a few cases in 2023 when elevated SO_2 emissions were seen in the hours prior to an explosive eruption. Such observations indicate that

higher temporal resolution SO_2 emission rates (e.g. hourly instead of daily) could help forecast explosive Shishaldin Volcano eruptions and further support the proposed model in which paroxysms are triggered by fast magma ascent/high magma fluxes into Shishaldin Volcano's reservoir (e.g., Parfit and Wilson, 1995; Vergniolle, 2024; this study). We caution, however, that SO_2 was rarely seen at the start of the 2019–2020 eruption, potentially suggesting that the early 2019–2020 eruptive material may have been already degassed or was smaller in volume, such that the utility of satellite SO_2 monitoring for Shishaldin Volcano may be eruption-specific. These observations further emphasize the importance of multidisciplinary data in volcano monitoring.

Finally, we saw substantial differences in CO_2 concentrations and in plume CO_2/SO_2 composition during several years of gas flights, with low CO_2/SO_2 ratios (<1–2) typically seen within eruptive periods, and a higher ratio (~11) seen during quiescence between eruptive periods. We hypothesize that this high inter-eruptive CO_2/SO_2 ratio indicates magma recharge by a deep, CO_2-rich magma (e.g., Burton et al., 2007; Aiuppa et al., 2007; Werner et al., 2013) and may be an early sign of future eruptive activity Shishaldin Volcano.

Moving forward, continued monitoring of SO_2 emissions using TROPOMI satellite data and adding complementary IASI observations during winter months (November - February) will help maximize sensitivity and consistency in satellite observations. Continued gas flight measurements whenever possible (ideally at least annually) will help constrain SO_2 emission rates (particularly if below satellite detection capabilities) and gas composition (e.g., CO_2/SO_2) to identify early signs of deep magma recharge. Finally, the installation of ground-based SO_2 monitoring instruments at Shishaldin Volcano, such as a scanning DOAS network (e.g., Galle et al., 2010; Arellano et al., 2021) or SO_2 camera (Kern et al., 2015; Aiuppa et al., 2023), or expanding the operational satellites used to include the complementary OMPS sensors, would increase the sensitivity and/or temporal rate of SO_2 emission rate monitoring, and thus potentially detect more subtle and/or short-lived anomalies to help forecast explosive eruptions.

5. Conclusions

We combine ultraviolet (UV) and infrared (IR) satellite SO_2 observations with airborne gas measurements, petrologic constraints, and degassing models to provide insights into magma degassing processes during Shishaldin Volcano's 2019–2020 and 2023 eruptions. We compare and combine TROPOMI and IASI SO_2 masses to robustly quantify Shishaldin Volcano's total eruptive SO_2 emissions. We find very good agreement between these sensors from spring to fall and note several missed wintertime detections by TROPOMI, due to limited wintertime UV, and note a general reduced sensitivity to low-

mass plumes by IASI. The combined TROPOMI and IASI satellite SO_2 dataset reveals that Shishaldin Volcano released ~6 times more SO_2 during its 2023 eruption relative to its 2019–2020 eruption (240 kt vs 40 kt, respectively). These observations combined with the petrologic method allow us to calculate degassed magma volumes of 4.17 x 10^6 m^3 and 29.7 x 10^6 m^3 for 2019–2020 and 2023 eruptions, respectively, indicating that the 2023 eruption was substantially larger than the 2019–2020 eruption. We observed highly variable SO_2 emission rates in TROPOMI data over the five-year study period from <100 to 85,000 t/d, which we attribute to a highly variable magma supply rate, consistent with existing models for basaltic paroxysms. We find that satellite-detectable SO_2 emissions are seen almost exclusively during or following periods of volcanic unrest and eruption, indicating that SO_2 degasses at relatively shallow depths at Shishaldin Volcano. Airborne gas CO_2/SO_2 ratios of <2 to 11 and degassing models suggest that magma degasses primarily at depths of <2–4 km below the surface during/following eruptions, and at depths ≥12 km between eruptions, indicating deep magma recharge in the months to years prior to the 2023 eruption. Collectively, these observations indicate that Shishaldin exhibits both open- and closed-system degassing behavior. We hypothesize that variations in degassing behavior and eruption style can be explained by differences in magma ascent rates, where low magma ascent rates lead to open-system degassing and weakly explosive to effusive eruptions, and high magma ascent rates lead to closed-system degassing and highly explosive eruptions. These findings indicate that satellite SO_2 observations combined with volcanic gas composition measurements provide unique insights into magmatic processes, can successfully track magma supply to the shallow crust, and have potential to help forecast highly explosive paroxysmal eruptions at Shishaldin Volcano and other analog volcanoes.

6. Supplementary information

Supplementary Materials A and B, as well as Figures S.1–S.7 can be found in the attached word document. Supplementary Tables S.1–S.13 can be found in the attached excel file.

7. Data Availability

All data supporting the findings of this study are available within the paper, its Supplementary Information, or existing data repositories as referenced within the paper. Specifically, TROPOMI SO_2 data used in this study are publicly available and accessible using the Sentinel Hub Catalog API (https://dataspace.copernicus.eu/analyse/apis/catalogue-apis). TROPOMI derived SO_2 masses and emission rates are from Loewen et al. 2026b. IASI data are from Clarisse et al. 2026. Airborne gas measurements are from AVO, 2026.

8. Acknowledgements

This research benefited from numerous insightful discussions with Alaska Volcano Observatory colleagues during and following the Shishaldin Volcano eruptions. This paper was substantially improved thanks to constructive reviews by Simon Carn, Adam Cotterill and Christine Sealing. Any use of trade, firm, or product names is for descriptive purposes only and does not imply endorsement by the U.S. Government.

9. Funding Statement

This study was supported through the Volcano Hazards Program of the U.S Geological Survey through the Alaska Volcano Observatory Cooperative Agreement No. G21AC10384 and National Science Foundation grant 1855126. B. Franco and L. Clarisse were were supported by the HIRS Prodex arrangement (ESA-BELSPO) and EUMETSAT (AC-SAF). L. Clarisse is Senior Research Associate supported by the Belgian F.R.S.-FNRS. N. Theys acknowledges financial support from ESA ATM-MPC S5P and Belgian Prodex TRACE-S5P projects.

10. References Cited

Aiuppa, A., Federico, C., Giudice, G., & Gurrieri, S. (2005). Chemical mapping of a fumarolic field: la Fossa crater, Vulcano Island (Aeolian Islands, Italy). *Geophysical Research Letters*, *32*(13). doi.org/10.1029/2005GL023207.

Aiuppa, A., Moretti, R., Federico, C., Giudice, G., Gurrieri, S., Liuzzo, M., Papale, P., Shinohara, H., & Valenza, M. (2007). Forecasting Etna eruptions by real-time observation of volcanic gas composition. *Geology*, *35*(12), 1115-1118. doi.org/10.1130/G24149A.1.

Aiuppa, A., Giudice, G., Gurrieri, S., Liuzzo, M., Burton, M., Caltabiano, T., McGonigle, A.J.S., Salerno, G., Shinohara, H., & Valenza, M. (2008). Total volatile flux from Mount Etna. *Geophysical Research Letters*, *35*(24). doi.org/10.1029/2008GL035871.

Aiuppa, A., Lo Bue Trisciuzzi, G., Alparone, S., Bitetto, M., Coltelli, M., Delle Donne, D., Ganci, G.,& Pecora, E. (2023). A SO2 flux study of the Etna volcano 2020–2021 paroxysmal sequences. *Frontiers in Earth Science*, *11*, 1115111. doi.org/10.3389/feart.2023.1115111.

Alaska Volcano Observatory (2026). Airborne Volcanic Gas Compositions and Emission Rates from Alaska Volcanoes. *U.S. Geological Survey data release*, doi.org/10.5066/P13IBC5P.

Allard, P., Burton, M., & Muré, F. (2005). Spectroscopic evidence for a lava fountain driven by previously accumulated magmatic gas. *Nature*, *433*(7024), 407-410. doi: 10.1038/nature03246.

Angarita, M., Grapenthin, R., Plank, S., Meyer, F. J., & Dietterich, H. (2022). Quantifying large-scale surface change using SAR amplitude images: Crater morphology changes during the 2019–2020 Shishaldin volcano eruption. *Journal of Geophysical Research: Solid Earth*, 127, e2022JB024344. doi.org/10.1029/2022JB024344.

Angarita, M., Grapenthin, R., Tan, D., Saunders-Shultz, P., Girona, T., Parameswaran, R. M., Lopez, T. M., Izbekov, P. E., Fee, D., Burgos, V., Moshrefzadeh, J. A., Shreve, T., & Larsen, J. (2026a). Multidisciplinary perspectives on Shishaldin Volcano: An open-system deforming volcano. *Bulletin of Volcanology*, 88, 111. doi.org/10.1007/s00445-026-01970-0.

Angarita, M. Wasser, V., Grapenthin, R., Lerner, A., Lopez, T., Parameswaran, R., Lyons, J. (2026b), Erupted volume during the 2014-2023 Semisopochnoi unrest and eruption constrained by multi-platform InSAR and volcanic gas observations, *Geochemistry, Geophysics, Geosystems*, 7, e2026GC013083. https://doi.org/10.1029/2026GC013083.

Arellano, S., Galle, B., Apaza, F., Avard, G., Barrington, C., Bobrowski, N., Bucarey, C., & Yalire, M. (2020). Synoptic analysis of a decade of daily measurements of SO2 emission in the troposphere from volcanoes of the global ground-based Network for Observation of Volcanic and Atmospheric Change. *Earth System Science Data Discussions*, *2020*, 1-33. doi.org/10.5194/essd-13-1167-2021.

Aubry, T.J., Engwell, S.L., Bonadonna, C., Mastin, L.G., Carazzo, G., Van Eaton, A.R., Jessop, D.E., Grainger, R.G., Scollo, S., Taylor, I.A. and Jellinek, A.M (2023), New insights into the relationship between mass eruption rate and volcanic column height based on the IVESPA data set. *Geophysical Research Letters*, *50*(14), p.e2022GL102633. doi.org/10.1029/2022GL102633.

Burton, M., Allard, P., Muré, F., & La Spina, A. (2007). Magmatic gas composition reveals the source depth of slug-driven Strombolian explosive activity. *Science*, *317*(5835), 227-230. doi.org/0.1126/science.1141900.

Burton, M., Hayer, C., Miller, C., & Christenson, B. (2021). Insights into the 9 December 2019 eruption of Whakaari/White Island from analysis of TROPOMI SO2 imagery. *Science Advances*, *7*(25), eabg1218. doi/org/10.1126/sciadv.abg1218

Carn, S. A., Krotkov, N. A., Yang, K., & Krueger, A. J. (2013). Measuring global volcanic degassing with the Ozone Monitoring Instrument (OMI). *Geological Society, London, Special Publications*, v. 380; p229-257. Doi.1144/SP380.12. doi.org/10.1016/j.jvolgeores.2016.01.002.

Carn, S. (2015), Multi-Satellite Volcanic Sulfur Dioxide L4 Long-Term Global Database V4, Greenbelt, MD, USA, Goddard Earth Science Data and Information Services Center (GES DISC), Accessed: [14 August 2026], doi.org/10.5067/MEASURES/SO2/DATA405.

Clarisse, L., Franco, B., Fabris, L., Theys, N., Hadji-Lazaro, J., Hurtmans, D., Clerbaux, C., and Coheur, P.-F. (2026). An 18-year record of atmospheric sulphur dioxide (SO2) derived from IASI measurements, *Earth System Science Data*, 18, 6667–6706, doi.org/10.5194/essd-18-6667-2026

Clerbaux, C., Boynard, A., Clarisse, L., George, M., Hadji-Lazaro, J., Herbin, H., Hurtmans, D., Pommier, M., Razavi, A., Turquety, S., Wespes, C., & Coheur, P. F. (2009). Monitoring of atmospheric composition using the thermal infrared IASI/MetOp sounder. *Atmospheric Chemistry and Physics*, *9*(16), 6041-6054. doi.org/10.5194/acp-9-6041-2009.

Coombs, M. L., Cameron, C. E., Dietterich, H. R., Boyce, E. S., Wech, A. G., Grapenthin, R., Wallace, K., Parker, T., Lopez, T., Crass, S., Haney, M. M., Ketner, D., Loewen, M. W., Lyons, J. J., Nakai, J. S., Power, J. A., Botnick, S., Brewster, I., Enders, M. L., Harmon, D., Kelly, P. J., & Randall, M. (2024). From field station to forecast: managing data at the Alaska Volcano Observatory. *Bulletin of Volcanology*, *86*(9), 79. doi.org/10.1007/s00445-024-01766-0.

Coppola, D., Laiolo, M., Franchi, A., Massimetti, F., Cigolini, C., & Lara, L. E. (2017). Measuring effusion rates of obsidian lava flows by means of satellite thermal data. *Journal of Volcanology and Geothermal Research*, *347*, 82-90. doi.org/10.1016/j.jvolgeores.2017.09.003.

Corradini, S., Guerrieri, L., Brenot, H., Clarisse, L., Merucci, L., Pardini, F., Prata, A. J., Realmuto, V. J., Stelitano, D., & Theys, N. (2021). Tropospheric volcanic SO2 mass and flux retrievals from satellite. The Etna December 2018 eruption. *Remote Sensing*, *13*(11), 2225. doi.org/10.3390/rs13112225.

Cotterill, A.S., Nicholson, E.J., Hayer, C.S.L. *et al.* Magma recharge at Manam volcano, Papua New Guinea, identified through thermal and SO_2 satellite remote sensing of

open-vent emissions (2024). *Bull Volcanol* **86**, 87. doi.org/10.1007/s00445-024-01772-2.

de Moor, J. M., Aiuppa, A., Avard, G., Wehrmann, H., Dunbar, N., Muller, C., Tamburello, G., Giudice, G., Liuzzo, M, Moretti, R., Conde, V., & Galle, B. (2016). Turmoil at Turrialba Volcano (Costa Rica): Degassing and eruptive processes inferred from high-frequency gas monitoring. *Journal of Geophysical Research: Solid Earth*, *121*(8), 5761-5775. doi.org/10.1002/2016JB013150.

Devine, J.D., Gardner, J.E., Brack, H.P., Layne, G.D. and Rutherford, M.J. (1995). Comparison of microanalytical methods for estimating H2O contents of silicic volcanic glasses. *American Mineralogist*, *80*(3-4), pp.319-328. doi.org/10.2138/am-1995-3-413

Di Genova, D., Brooker, R.A., Mader, H.M., Drewitt, J.W., Longo, A., Deubener, J., Neuville, D.R., Fanara, S., Shebanova, O., Anzellini, S. and Arzilli, F. (2020), In situ observation of nanolite growth in volcanic melt: A driving force for explosive eruptions. *Science advances*, *6*(39), p.eabb0413. doi.or/10.1126/sciadv.abb0413.

Ding, S., Plank, T., Wallace, P. J., & Rasmussen, D. J. (2023). Sulfur_X: A model of sulfur degassing during magma ascent. *Geochemistry, Geophysics, Geosystems*, *24*(4), e2022GC010552. doi.org/10.1029/2022GC010552.

Doukas, M.P. (2002). A new method for GPS-based wind speed determinations during airborne volcanic plume measurements: U.S. Geological Survey Open-File Report 02-395, 13 p.

Edmonds, M., Oppenheimer, C., Pyle, D. M., Herd, R. A., & Thompson, G. (2003a). SO2 emissions from Soufrière Hills Volcano and their relationship to conduit permeability, hydrothermal interaction and degassing regime. *Journal of Volcanology and Geothermal Research*, *124*(1-2), 23-43. doi.org/10.1016/S0377-0273(03)00041-6.

Edmonds, M., Herd, R. A., Galle, B., & Oppenheimer, C. M. (2003b). Automated, high time-resolution measurements of SO2 flux at Soufriere Hills Volcano, Montserrat. *Bulletin of Volcanology*, *65*(8), 578-586. doi.org/10.1007/s00445-003-0286-x.

Edmonds, M., & Woods, A. W. (2018). Exsolved volatiles in magma reservoirs. *Journal of Volcanology and Geothermal Research*, *368*, 13-30. doi.org/10.1016/j.jvolgeores.2018.10.018.

Edmonds, M., Liu, E.J. and Cashman, K.V., 2022. Open-vent volcanoes fueled by depth-integrated magma degassing. *Bulletin of Volcanology*, *84*(3), p.28. doi.org/10.1007/s00445-021-01522-8.

Esse, B., Burton, M., Hayer, C., La Spina, G., Pardo Cofrades, A., Asensio-Ramos, M., Barrancos, J., & Pérez, N. (2025a). Forecasting the evolution of the 2021 Tajogaite eruption, La Palma, with TROPOMI/PlumeTraj-derived SO2 emission rates. *Bulletin of Volcanology*, *87*(3), 20. doi.org/10.1007/s00445-025-01803-6.

Esse, B., Burton, M., Brenot, H., & Theys, N. (2025b). Insights into eruption dynamics from TROPOMI/PlumeTraj-derived SO2 emissions during the 2022 eruption of Mauna Loa, Hawai'i. *Bulletin of Volcanology*, *87*(9), 69.doi.org/10.1007/s00445-025-01839-8.

Ewert, J. W., Diefenbach, A. K., & Ramsey, D. W. (2018). 2018 update to the US Geological Survey national volcanic threat assessment, U.S. Geological Survey *Scientific Investigations Report 2018-5140*. doi.org/10.3133/sir20185140.

Fee, D., Tan, D., Haney, M., Merritt, K., Lyons, J., Wech, A., Loewen, M., Boyce, E., & Scamfer, L. (2026). Seismic and infrasound signals from the 2023 explosive eruption sequence of Shishaldin Volcano, Alaska, *Bulletin of Volcanology*, 88, 111. doi.org/10.1007/s00445-026-01951-3.

Fischer, T. P., Roggensack, K., & Kyle, P. R. (2002). Open and almost shut case for explosive eruptions: Vent processes determined by SO2 emission rates at Karymsky volcano, Kamchatka. *Geology*, *30*(12), 1059-1062. doi.org/10.1130/0091-7613(2002)030<1059:OAASCF>2.0.CO;2.

Galle, B., Oppenheimer, C., Geyer, A., McGonigle, A. J., Edmonds, M., & Horrocks, L. (2003). A miniaturised ultraviolet spectrometer for remote sensing of SO2 fluxes: a new tool for volcano surveillance. *Journal of Volcanology and Geothermal Research*, *119*(1-4), 241-254. doi.org/10.1016/S0377-0273(02)00356-6.

Galle, B., Johansson, M., Rivera, C., Zhang, Y., Kihlman, M., Kern, C., Lehmann, T., Platt, U., Arellano, S., & Hidalgo, S. (2010). Network for Observation of Volcanic and Atmospheric Change (NOVAC)—A global network for volcanic gas monitoring: Network layout and instrument description. *Journal of Geophysical Research: Atmospheres*, *115*(D5). doi.org/10.1029/2009JD011823.

Gardner, C.A., and Guffanti, M.C., (2006), U.S. Geological Survey's alert-notification system for volcanic activity (ver. 2.0, April 2025): U.S. Geological Survey Fact Sheet 2006–3139, 4 p., https://doi.org/10.3133/fs20063139.

Gerlach, T. M. (1986), Exsolution of H_2O, CO_2, and S during eruptive episodes at Kilauea Volcano, Hawaii, *J. Geophys. Res.*, 91(B12), 12177–12185, doi.or/10.1029/JB091iB12p12177.

Gerlach, T. M., Westrich, H. R., Casadevall, T. J., & Finnegan, D. L. (1994). Vapor saturation and accumulation in magmas of the 1989–1990 eruption of Redoubt Volcano, Alaska. *Journal of Volcanology and Geothermal Research*, *62* (1-4), 317-337. doi.org/10.1016/0377-0273(94)90039-6.

Gerlach, T. M., McGee, K. A., Sutton, A. J., & Elias, T. (1998). Rates of volcanic CO_2 degassing from airborne determinations of SO_2 emission rates and plume CO_2/SO_2: Test study at Pu‘u ‘Ō‘ō Cone, Kīlauea Volcano, Hawai‘i. *Geophysical Research Letters*. doi.org/10.1029/98GL02030.

Giggenbach, W. F. (1996). Chemical composition of volcanic gases. In *Monitoring and mitigation of volcano hazards* (pp. 221-256). Berlin, Heidelberg: Springer Berlin Heidelberg. doi.org/10.1007/978-3-642-80087-0_7.

Gomez-Patron, A., Dietterich, H., Schneider, D., (this issue), Using remote sensing to analyze pre- and co-paroxysm processes at Shishaldin Volcano to improve short-term hazard forecasting. *Bulletin of Volcanology*, 88, 111. https://10.1007/s00445-026-02033-0.

Harris, A. J., Flynn, L. P., Keszthelyi, L., Mouginis-Mark, P. J., Rowland, S. K., & Resing, J. A. (1998). Calculation of lava effusion rates from Landsat TM data. *Bulletin of Volcanology*, *60*(1), 52-71. doi.org/10.1007/s004450050216.

Iacono-Marziano, G., Morizet, Y., Le Trong, E., & Gaillard, F. (2012). New experimental data and semi-empirical parameterization of H2O–CO2 solubility in mafic melts. *Geochimica et Cosmochimica Acta*, *97*, 1-23. doi.org/10.1016/j.gca.2012.08.035.

Izbekov, P. E., Loewen, M., Lubbers, J., Waythomas, C., Wallace, K. (2027), Bulk-Rock, Glass, and Mineral Compositions of Eruptive Products from the 2023 Eruption of Shishaldin Volcano, Alaska, Version 1.0. *Interdisciplinary Earth Data Alliance (IEDA)*. https://doi.org/10.60520/IEDA/114645. Accessed 2026-09-30.

Jaupart, C., & Vergniolle, S. (1989). The generation and collapse of a foam layer at the roof of a basaltic magma chamber. *Journal of fluid mechanics*, *203*, 347-380. doi.org/10.1017/S0022112089001497.

Kelly, P. J., Kern, C., Roberts, T. J., Lopez, T., Werner, C., & Aiuppa, A. (2013). Rapid chemical evolution of tropospheric volcanic emissions from Redoubt Volcano, Alaska, based on observations of ozone and halogen-containing gases. *Journal of Volcanology and Geothermal Research*, *259*, 317-333. doi.org/10.1016/j.jvolgeores.2012.04.023.

Kern, C., Lübcke, P., Bobrowski, N., Campion, R., Mori, T., Smekens, J. F., Stebel, K., Tamburello, G., Burton, M., Platt, U., & Prata, F. (2015). Intercomparison of SO2 camera systems for imaging volcanic gas plumes. *Journal of Volcanology and Geothermal Research*, *300*, 22-36. doi.org/10.1016/j.jvolgeores.2014.08.026

Kern, C., Lerner, A. H., Elias, T., Nadeau, P. A., Holland, L., Kelly, P. J., Werner, C.A., Clor, L.E., & Cappos, M. (2020). Quantifying gas emissions associated with the 2018 rift eruption of Kīlauea Volcano using ground-based DOAS measurements. *Bulletin of Volcanology*, *82*(7), 55. doi.org/10.1007/s00445-020-01390-8.

Kern, C. (2025). Ultraviolet and visible remote sensing of volcanic gas emissions. *Journal of Volcanology and Geothermal Research*, 108423. doi.org/10.1016/j.jvolgeores.2025.108423.

Kilbride, B. M., Edmonds, M., & Biggs, J. (2016). Observing eruptions of gas-rich compressible magmas from space. *Nature Communications*, *7*(1), 13744. doi.org/10.1038/ncomms13744.

Kraus, S. (2006) DOASIS – A Framework Design for DOAS. PhD Thesis, University of Mannheim, https://www.shaker.eu/en/content/catalogue/index.asp?lang=en&ID=8&ISBN=978-3-8322-5452-0

Lerner, A.H., Wallace, P.J., Shea, T., Mourey, A.J., Kelly, P.J., Nadeau, P.A., Elias, T., Kern, C., Clor, L.E., Gansecki, C., Lee, R.L., Moore, L.R., Werner, C.A. (2021). The petrologic and degassing behavior of sulfur and other magmatic volatiles from the 2018 eruption of Kīlauea, Hawai‘i: melt concentrations, magma storage depths, and magma recycling. *Bulletin of Volcanology*, 83, 43. doi.org/10.1007/s00445-021-01459-y.

Loewen, M., Orr, T., Lopez, T., Fee, D., Gomez-Patron, A., Dietterich, H., Wallace, K., & Haney, M., Overview and chronology of the 2019-2020 and 2023 eruptions of Shishaldin Volcano (2026a), *Bulletin of Volcanology*, 88, 111.

Loewen, M. W., Gomez-Patron, A., Fee, D., Lopez, T., Mota, R., Saunders-Shultz, P., Merritt, K., Dietterich, H., Brewster, I., Wallace, K. (2026b). Shishaldin Volcano 2019-2020 and 2023 Eruption Chronology Data, Alaska Division of Geological & Geophysical Surveys Raw Data File 2026-15. doi.org/10.14509/32077.

Lopez, T., Carn, S., Werner, C., Fee, D., Kelly, P., Doukas, M., Pfeffer, M., Webley, P., Cahill, C. & Schneider, D. (2013). Evaluation of Redoubt Volcano's sulfur dioxide

emissions by the Ozone Monitoring Instrument. *Journal of Volcanology and Geothermal Research*, *259*, 290-307. doi.org/10.1016/j.jvolgeores.2012.03.002.

Lopez, T., Clarisse, L., Schwaiger, H., Van Eaton, A., Loewen, M., Fee, D., Lyons, J., Wallace, K., Searcy, C., Wech, A., Haney, M., Schneider, D., & Graham, N. (2020). Constraints on eruption processes and event masses for the 2016–2017 eruption of Bogoslof volcano, Alaska, through evaluation of IASI satellite SO2 masses and complementary datasets. *Bulletin of Volcanology*, *82*(2), 17. doi.org/10.1007/s00445-019-1348-z.

Lyons, J. J., Tan, D., Angarita, M., Loewen, M. W., Lopez, T., Grapenthin, R., Hotovec-Ellis, A. J., Fee, D., & Haney, M. M. (2025). Identifying precursors and tracking pulses of magma ascent in multidisciplinary data during the 2018–2023 phreatomagmatic eruption at Semisopochnoi Island, Alaska. *Journal of Volcanology and Geothermal Research*, *463*, 108329. doi.org/10.1016/j.jvolgeores.2025.108329.

Mastin, L.G. (2014), Testing the accuracy of a 1-D volcanic plume model in estimating mass eruption rate. *Journal of Geophysical Research: Atmospheres*, *119*(5), pp.2474-2495. doi.org/10.1002/2013JD020604.

Mota, R., Van Eaton, A.R., Mastin, L., Schneider, D., Dietterich, H., Pacheco, J., Artur, G. (this issue). Satellite observations, plume dynamics, and volcanic lightning from the 2023 eruption of Shishaldin Volcano, Alaska. *Bulletin of Volcanology,* 88, 111. doi.org/10.1007/s00445-026-02030-3.

Nye, C., Keith, T., Eichelberger, J., Miller, T., McNutt, S., Moran, S., Schneider, D., Dehn., J., & Schaefer, J. (2002). The 1999 eruption of Shishaldin Volcano, Alaska: monitoring a distant eruption. *Bulletin of Volcanology*, *64*(8), 507-519. doi.org/10.1007/s00445-002-0225-2.

O'Neill, H. S. C., & Mavrogenes, J. A. (2022). The sulfate capacities of silicate melts. *Geochimica et Cosmochimica Acta*, 334, 368–382. doi.org/10.1016/j.gca.2022.06.020.

Oppenheimer, C., Scaillet, B., & Martin, R. S. (2011). Sulfur degassing from volcanoes: source conditions, surveillance, plume chemistry and earth system impacts. *Reviews in mineralogy and geochemistry*, *73*(1), 363-421. doi.org/10.2138/rmg.2011.73.13.

Orr, T. R., Cameron, C. E., Dietterich, H. R., Dixon, J. P., Enders, M. L., Grapenthin, R., Iezzi, A.M., Loewen, M.W., Power, J.A., Searcy, C., Tepp, G., Toney, L., Waythomas, C.F., & Wech, A. G. (2023). 2019 Volcanic activity in Alaska—Summary of events and

response of the Alaska Volcano Observatory, U.S. Geological Survey Scientific Investigations Report 2023-5039. doi.org/10.3133/sir20235039.

Orr, T.R., Cameron, C.C., Dietterich, H., Loewen, M., Lopez, T., Lyons, J., Nakai, J., Power, J., Searcy, C., Tepp, G., & Waythomas, C., (2024). 2020 Volcanic activity in Alaska—Summary of events and response of the Alaska Volcano Observatory, *U.S. Geological Survey Scientific Investigations Report 2024-5004*. doi.org/10.3133/sir20245004.

Parfitt, E.A. and Wilson, L. (1995). Explosive volcanic eruptions—IX. The transition between Hawaiian-style lava fountaining and Strombolian explosive activity. *Geophysical Journal International*, *121*(1), pp.226-232. doi.org/10.1111/j.1365-246X.1995.tb03523.x.

Parfitt, E.A., 2004. A discussion of the mechanisms of explosive basaltic eruptions. *Journal of Volcanology and Geothermal Research*, *134*(1-2), pp.77-107. doi.org/10.1016/j.jvolgeores.2004.01.002.

Pfeffer, M. A., Arellano, S., Barsotti, S., Petersen, G. N., Barnie, T., Ilyinskaya, E., Hjorvar, T., Bali, E., Pedersen, G., Gudmundsson, G., Vogfjord, K., Ranta, E. J., Oladottir, B., Edwards, B., Mousallam, Y., Stefansson, A., Scott, S. W., Smekens, J.F., Varnam, M., Titos, M. (2024). SO2 emission rates and incorporation into the air pollution dispersion forecast during the 2021 eruption of Fagradalsfjall, Iceland. *Journal of Volcanology and Geothermal Research*, *449*, p.108064. doi.org/10.1016/j.jvolgeores.2024.108064

Platt, U., & Stutz, J. (2008). Differential absorption spectroscopy. In *Differential Optical Absorption Spectroscopy: Principles and Applications* (pp. 135-174). Berlin, Heidelberg: Springer Berlin Heidelberg. doi.org/10.1007/978-3-540-75776-4.

Queißer, M., Burton, M., Theys, N., Pardini, F., Salerno, G., Caltabiano, T., Varnam, M., Esse, B., & Kazahaya, R. (2019). TROPOMI enables high resolution SO2 flux observations from Mt. Etna, Italy, and beyond. *Scientific reports*, *9*(1), 957. doi.org/10.1038/s41598-018-37807-w.

Rasmussen, D. J., Plank, T. A., Roman, D. C., Power, J. A., Bodnar, R. J., & Hauri, E. H. (2018). When does eruption run-up begin? Multidisciplinary insight from the 1999 eruption of Shishaldin volcano. *Earth and Planetary Science Letters*, *486*, 1-14. doi.org/10.1016/j.epsl.2018.01.001.

Realmuto, V. J., Abrams, M. J., Buongiorno, M. F., & Pieri, D. C. (1994). The use of multispectral thermal infrared image data to estimate the sulfur dioxide flux from volcanoes: A case study from Mount Etna, Sicily, July 29, 1986. *Journal of Geophysical Research: Solid Earth*, *99*(B1), 481-488. doi.org/10.1029/93JB02062.

Shinohara, H. (2008). Excess degassing from volcanoes and its role on eruptive and intrusive activity. *Reviews of Geophysics*, *46*(4). doi.org/10.1029/2007RG000244.

Saunders-Shultz, P., Lopez, T., Dietterich, H., & Girona, T. (2024). Automatic identification and quantification of volcanic hotspots in Alaska using HotLINK—The hotspot learning and identification network. *Frontiers in Earth Science*, 12, 1345104. doi.org/10.3389/feart.2024.1345104.

Stelling, P.L., 2003. Volcanism on Unimak Island, Alaska, USA: A petrologic focus on Shishaldin and Fisher Volcanoes. University of Alaska Fairbanks.

Sutton, A. J., Elias, T., & Kauahikaua, J. (2003). Lava-Effusion Rates for the Pu‘u ‘Õ‘ō-Kūpaianaha Eruption Derived from SO2, Emissions and Very Low Frequency (VLF) Measurements. In: The Pu‘u ‘Ō‘ō-Kūpaianaha Eruption of Kīlauea Volcano, Hawai‘i: The First 20 Years, *U.S. Geological Survey Professional Paper 1676*, Chapter 8, 137-148.

Symonds, R.B., Gerlach, T.M. and Reed, M.H. (2001), Magmatic gas scrubbing: implications for volcano monitoring. *Journal of Volcanology and Geothermal Research*, *108*(1-4), pp.303-341. doi.org/10.1016/S0377-0273(00)00292-4.

Taylor, I. A., Preston, J., Carboni, E., Mather, T. A., Grainger, R. G., Theys, N., Hidalgo, S., & Kilbride, B. M. (2018). Exploring the utility of IASI for monitoring volcanic SO2 emissions. *Journal of Geophysical Research: Atmospheres*, *123*(10), 5588-5606. doi.org/10.1002/2017JD027109.

Theys, N., De Smedt, I., Yu, H., Danckaert, T., van Gent, J., Hörmann, C., ... & Van Roozendael, M. (2017). Sulfur dioxide retrievals from TROPOMI onboard Sentinel-5 Precursor: algorithm theoretical basis. *Atmospheric Measurement Techniques*, *10*(1), 119-153. doi.org/10.5194/amt-10-119-2017.

Theys, N., Hedelt, P., De Smedt, I., Lerot, C., Yu, H., Vlietinck, J., Pedergnana, M., Arellano, S., Galle, B., Dernandez, D. Carlito, C.J.M., Barrington, C., Taisne, B., Delgado-Granados, H., Loyola, D., & Van Roozendael, M. (2019). Global monitoring of volcanic SO2 degassing with unprecedented resolution from TROPOMI onboard

Sentinel-5 Precursor. *Scientific reports*, *9*(1), 2643. doi.org/10.1038/s41598-019-39279-y.

Vergniolle, S. (2024). Origin of basaltic subplinian eruption at Shishaldin volcano (Alaska): a vigorously degassing magma reservoir hosting small bubbles. *Journal of Geophysical Research: Solid Earth*, *129*(8), e2023JB028161. doi.org/10.1029/2023JB028161.

Waythomas, C., Loewen M., Dietterich, H., (this issue). Syneruptive Edifice Subsidence during the 2023 Eruption of Shishaldin Volcano, Alaska. *Bulletin of Volcanology*, 88, 111.

Werner, C., Kelly, P. J., Doukas, M., Lopez, T., Pfeffer, M., McGimsey, R., & Neal, C. (2013). Degassing of CO2, SO2, and H2S associated with the 2009 eruption of Redoubt Volcano, Alaska. *Journal of Volcanology and Geothermal Research*, *259*, 270-284. doi.org/10.1016/j.jvolgeores.2012.04.012.

Werner, C., Kern, C., Coppola, D., Lyons, J. J., Kelly, P. J., Wallace, K. L., Schnieder, D., & Wessels, R. L. (2017). Magmatic degassing, lava dome extrusion, and explosions from Mount Cleveland volcano, Alaska, 2011–2015: Insight into the continuous nature of volcanic activity over multi-year timescales. *Journal of Volcanology and Geothermal Research*, *337*, 98-110. doi.org/10.1016/j.jvolgeores.2017.03.001.

Werner, C., Rasmussen, D. J., Plank, T., Kelly, P. J., Kern, C., Lopez, T., Gliss, J., Power, J. A., Roman, D. C., Izbekov, P., & Lyons, J. (2020). Linking subsurface to surface using gas emission and melt inclusion data at Mount Cleveland volcano, Alaska. *Geochemistry, Geophysics, Geosystems*, *21*(7), e2019GC008882. doi.org/10.1029/2019GC008882.

Wilson, L. and Head III, J.W. (1981), Ascent and eruption of basaltic magma on the Earth and Moon. *Journal of Geophysical Research: Solid Earth*, *86*(B4), pp.2971-3001. doi.org/10.1029/JB086iB04p02971.

2020 Census Data. State of Alaska, Department of Labor and Workforce Development. Retrieved 14 September 2026. https://live.laborstats.alaska.gov/cen/2020-census-data.html.

Supplementary Material for:

Insights into magmatic processes at Shishaldin Volcano based on satellite and airborne volcanic gas measurements and magma degassing models

Taryn Lopez, University of Alaska Fairbanks Geophysical Institute, Alaska Volcano Observatory, 0000-0001-6831-4573
Allan Lerner, U.S. Geological Survey, Cascades Volcano Observatory, Vancouver, WA, USA, 0000-0001-7208-1493.
Bruno Franco, Université libre de Bruxelles (ULB), BLU–ULB research Center, Spectroscopy, Quantum Chemistry and Atmospheric Remote Sensing (SQUARES), Brussels, Belgium, 0000-0003-0736-458X
Matthew W. Loewen, U.S. Geological Survey, Alaska Volcano Observatory, Anchorage, Alaska, 0000-0002-5621-285X
Peter Kelly, U.S. Geological Survey, Cascades Volcano Observatory, Vancouver, WA, USA, 0000-0002-3868-1046
Christoph Kern, U.S. Geological Survey, Cascades Volcano Observatory, Vancouver, WA, USA, 0000-0002-8920-5701
Laura Clor, U.S. Geological Survey, Cascades Volcano Observatory, Vancouver, WA, USA, 0000-0003-2633-5100.
Cynthia Werner, U.S. Geological Survey (contractor), New Plymouth, New Zealand, 0000-0003-3311-6694.
Lieven Clarisse, Université libre de Bruxelles (ULB), BLU–ULB research Center, Spectroscopy, Quantum Chemistry and Atmospheric Remote Sensing (SQUARES), Brussels, Belgium, 0000-0002-8805-2141
Daniel Rasmussen, Peregrine Advisors, Silver Spring, MD, USA, 0000-0003-0137-6715
Valerie Wasser, University of Alaska Fairbanks Geophysical Institute, Alaska Volcano Observatory, 0000-0001-9786-9770
Skye Kushner, University of Alaska Anchorage, Anchorage, Alaska
Pablo Saunders-Shultz, U.S. Geological Survey, Alaska Volcano Observatory, Anchorage, Alaska, 0009-0009-4096-9821
Israel Brewster, University of Alaska Fairbanks Geophysical Institute, Alaska Volcano Observatory, Anchorage, Alaska
Nicolas Theys, Royal Belgian Institute for Space Aeronomy (BIRA-IASB), Brussels, Belgium
Pavel Izbekov, University of Alaska Fairbanks Geophysical Institute, Alaska Volcano Observatory, 0000-0001-9052-7655

Corresponding Author: Taryn Lopez, tmlopez@alaska.edu

Supplementary Methods Text:

- Supplement A: Analytical Routine for Sulfur Wavescans
- Supplement B: Viscosity Calculations
- References

Supplementary Figures:

- **Figure S.1:** Timeseries comparison between SO_2 plume heights derived from TROPOspheric Monitoring Instrument (TROPOMI, purple) and Infrared Atmospheric Sounding Interferometer (IASI, blue) for the (a) 2019–2020 and (b) 2023 eruptions of Shishaldin Volcano.

- **Figure S.2:** Comparison between coincident IASI and TROPOMI Shishaldin Volcano SO_2 masses (left) and plume heights (right) throughout 2019−2020 and 2023 eruptive episodes as a function the time difference between TROPOMI and IASI overpass times in hours.

- **Figure S.3**: Total SO_2 masses calculated by IASI (left) and TROPOMI (right) showing proportions of matched (blue) and unmatched (red) detections, where matches represent TROPOMI and IASI detections of SO_2 from Shishaldin Volcano acquired within 3.3 hours of each other.

- **Figure S.4:** Bar diagrams for the 2019−2020 (left) and 2023 (right) Shishaldin eruptions showing cumulative eruptive SO_2 mass determined from IASI only (blue), TROPOMI only (purple), and the best combined mass (largest per day) derived from either IASI or TROPOMI sensors (yellow).

- **Figure S.5:** Sulfur_X open-system (A) and closed-system (B) degassing model results (see Figs. 9, 10) of (left) S and CO_2 in the melt and (right) S and H_2O in the melt shown in blue, compared to measured melt inclusions from Rasmussen et al. (2018). In both scenarios, the modeled melt is assumed to be 1120°C, fO_2 = ΔFQM+0.9 (S^{6+}/S^{total} 0.3−0.4), and to initially contain 1710 ppm S and 2.5 wt% H_2O.

- **Figure S.6:** Empirical degassing model fit to measured volatiles in melt inclusions from Shishaldin Volcano's 1999 eruption.

- **Figure S.7:** Sulfur_X open-system isothermal degassing model for a Shishaldin Volcano's basaltic melt using the CO_2-H_2O degassing model of Iacono-Marziano et al. (2012), showing the ratios of accumulated exsolved gases (compared to

Fig. 10 of the main text, which shows instantaneous gas ratios for each pressure step).

Supplementary Methods Text:

Supplement A: Analytical Routine for Sulfur Wavescans

Twenty-seven representative melt inclusions (>50 μm in diameter) hosted in olivine and plagioclase phenocrysts were selected for sulfur analysis. The analytical routine consisted of two steps: (1) determination of the sulfur Kα peak position via wavelength scanning (wave scan analysis), and (2) quantitative point analysis of sulfur at the determined peak position, conducted simultaneously with major element analysis.

Both wave scan analysis and point analysis were performed using a JEOL JXA-8530F electron microprobe housed at the Advanced Instrumentation Laboratory, Geophysical Institute, University of Alaska Fairbanks. Petrographic thin sections were polished and carbon-coated to a thickness of ca. 250 Å. Wave scans were acquired using an accelerating voltage of 15 kV, a beam current of 50 nA, and a focused beam. Characteristic X-ray intensities were collected simultaneously on three PETL spectrometers. For each wave scan analysis, intensities were measured over 30 steps with a 0.01 mm JEOL spectrometer movement increment (corresponding to a wavelength interval of 0.00031 Å) and a dwell time of 60 seconds per step. The wavelength scan range for each PETL spectrometer was defined individually based on the positions of the S^{6+} and S^{2-} Kα peaks, determined by peaking on reference standards (Taylor Gypsum and Taylor Pyrite, respectively). The selected scan range encompassed both peak positions and adjacent background regions, extending ±0.10 mm beyond the peak limits.

The acquired sulfur Kα wave scans were processed by fitting Gaussian functions to the measured intensity distributions. The position of the sulfur Kα peak in unknown samples, relative to those of S^{6+} and S^{2-} in reference materials, was used to determine sulfur speciation. Oxygen fugacity was subsequently calculated following equation 18 of Jugo et al. (2005). Results from three spectrometers were averaged and are reported in Table S.5.

Point analyses for major oxides and sulfur were performed in 1-6 spots adjacent to the wave scan spot within the same melt inclusion, using a 15 keV accelerating voltage, a 10 nA beam current, and a 5-μm-diameter beam. Sodium and aluminum were analyzed

first, with a time-dependent intensity correction applied to minimize volatilization effects (Nielsen and Sigurdsson, 1981). Sulfur Kα characteristic X-rays were acquired on PETL crystal mounted on spectrometer 2, which exhibited the highest sensitivity to sulfur among all three PETL spectrometers used in this study. Because the determined sulfur Kα peak positions exhibited minimal variability across all measured melt inclusions, the averaged sulfur Kα peak position on spectrometer 2's PETL crystal was used for all quantitative point analyses. Details on the analytical conditions used in point analyses and the complete dataset with sample descriptions can be found in Izbekov et al. (2027).

Supplement B: Viscosity Calculations

Viscosity for Shishaldin Volcano's 2023 magma was calculated using petrologic constraints from Izbekov et al. (2027) and the Conflow program by Mastin and Ghiorso (2000) and Mastin, (2002). Temperatures of 1066 and 1109 °C were used, corresponding to the minimum and maximum temperatures determined from ilmenite–magnetite pairs in the Ol–Opx–Pl enclave found in the 2023 Shishaldin Volcano eruptive products (Izbekov et al., 2027). An average crystallinity of 20 vol.% was used based on modal analyses of the erupted products. A pressure of 26 MPa and 1 wt.% H_2O were used as representative example values for shallow conduit conditions. The calculated viscosities are 208.6 and 125.5 Pa·s at 1066 and 1109 °C, respectively.

References

Angarita, M., Grapenthin, R., Tan, D., Saunders-Shultz, P., Girona, T., Parameswaran, R. M., Lopez, T. M., Izbekov, P. E., Fee, D., Burgos, V., Moshrefzadeh, J. A., Shreve, T., & Larsen, J. (2026a), Multidisciplinary perspectives on Shishaldin Volcano: An open-system deforming volcano. *Bulletin of Volcanology*, 88, 111. doi.org/10.1007/s00445-026-01970-0.

Iacono-Marziano, G., Morizet, Y., Le Trong, E., & Gaillard, F. (2012). New experimental data and semi-empirical parameterization of H2O–CO2 solubility in mafic melts. *Geochimica et Cosmochimica Acta*, *97*, 1-23. doi.org/10.1016/j.gca.2012.08.035.

Izbekov, P. E., Loewen, M., Lubbers, J., Waythomas, C., Wallace, K. (2027), Bulk-Rock, Glass, and Mineral Compositions of Eruptive Products from the 2023 Eruption of

Shishaldin Volcano, Alaska, Version 1.0. *Interdisciplinary Earth Data Alliance (IEDA)*. https://doi.org/10.60520/IEDA/114645. Accessed 2026-09-30.

Jugo, P. J., Luth, R. W., & Richards, J. P. (2005), Experimental data on the speciation of sulfur as a function of oxygen fugacity in basaltic melts. *Geochimica et Cosmochimica Acta*, 69(2), 497-503. doi.org/10.1016/j.gca.2004.07.011

Mastin, L.G. and Ghiorso, M.S. (2000), A numerical program for steady-state flow of magma-gas mixtures through vertical eruptive conduits (No. 2000-209). U.S. Geological Survey Open-File Report 2000-209. doi.org/10.3133/ofr00209.

Mastin, L.G. (2002), Insights into volcanic conduit flow from an open-source numerical model. *Geochemistry, Geophysics, Geosystems*, *3*(7), pp.1-18. doi.org/10.1029/2001GC000192.

Nielsen, C. H., & Sigurdsson, H. (1981), Quantitative methods for electron microprobe analysis of sodium in natural and synthetic glasses. *American Mineralogist*, 66(5-6), 547-552.

Rasmussen, D. J., Plank, T. A., Roman, D. C., Power, J. A., Bodnar, R. J., & Hauri, E. H. (2018), When does eruption run-up begin? Multidisciplinary insight from the 1999 eruption of Shishaldin volcano. *Earth and Planetary Science Letters*, *486*, 1-14. doi.org/10.1016/j.epsl.2018.01.001.

Werner, C., Rasmussen, D. J., Plank, T., Kelly, P. J., Kern, C., Lopez, T., Gliss, J., Power, J. A., Roman, D. C., Izbekov, P., & Lyons, J. (2020), Linking subsurface to surface using gas emission and melt inclusion data at Mount Cleveland volcano, Alaska. *Geochemistry, Geophysics, Geosystems*, *21*(7), e2019GC008882. doi.org/10.1029/2019GC008882.

Supplementary Figures:

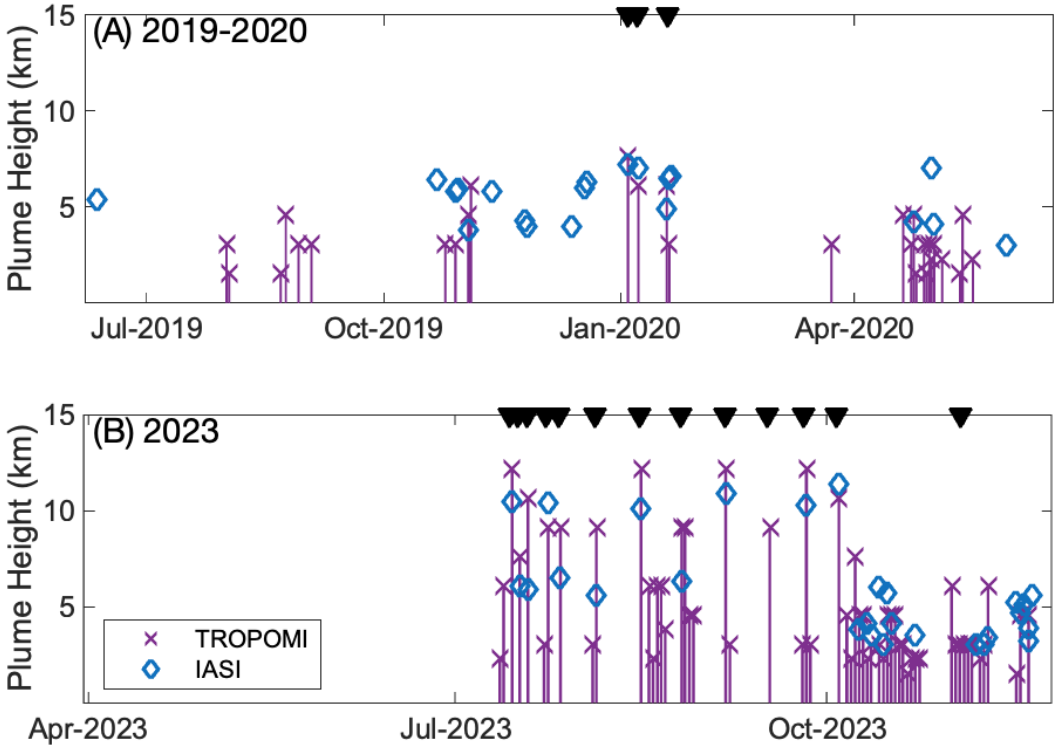


Figure S.1: Timeseries comparison between SO_2 plume heights derived from TROPOspheric Monitoring Instrument (TROPOMI, purple) and Infrared Atmospheric Sounding Interferometer (IASI, blue) for the (a) 2019–2020 and (b) 2023 eruptions of Shishaldin Volcano.

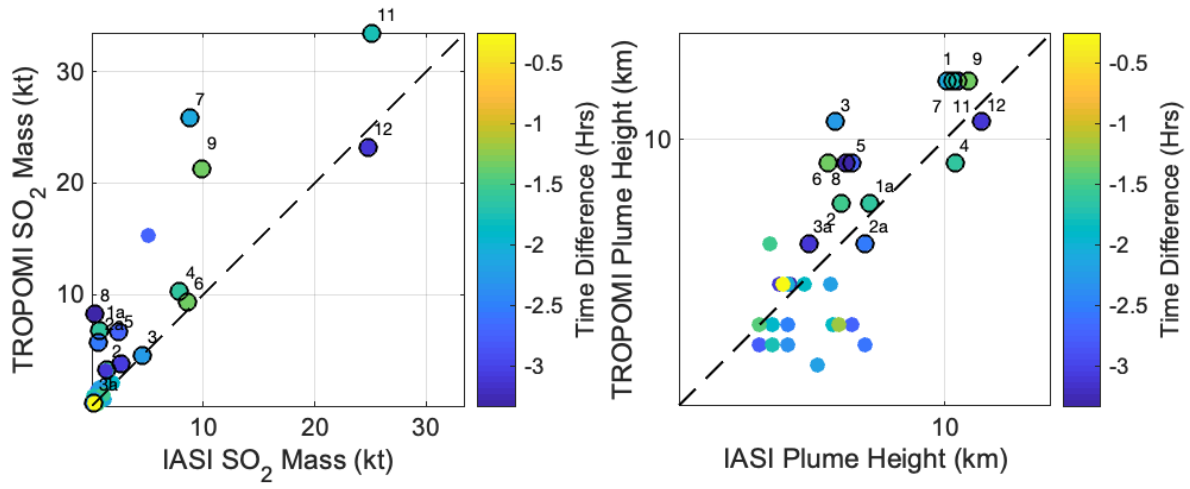


Figure S.2: Comparison between coincident IASI and TROPOMI Shishaldin Volcano SO_2 masses (left) and plume heights (right) throughout 2019−2020 and 2023 eruptive episodes as a function the time difference between TROPOMI and IASI overpass times in hours. Dashed black lines indicate a 1:1 agreement. All detections associated with paroxysmal events are labeled, with the 2019−2020 eruption events distinguished as "a."

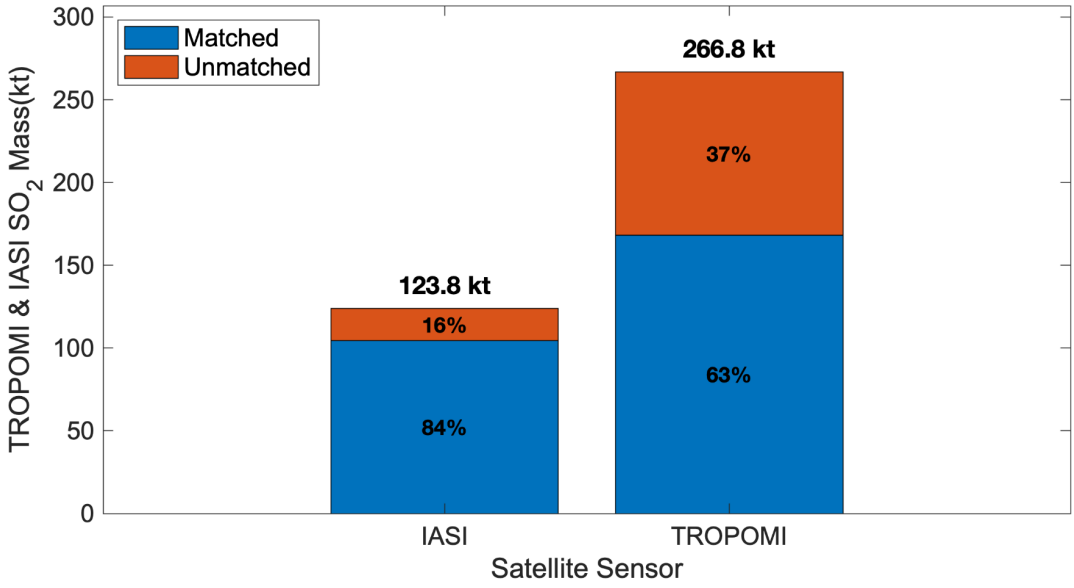


Figure S.3: Total SO_2 masses calculated by IASI (left) and TROPOMI (right) showing proportions of matched (blue) and unmatched (red) detections, where matches

represent TROPOMI and IASI detections of SO_2 from Shishaldin Volcano acquired within 3.3 hours of each other.

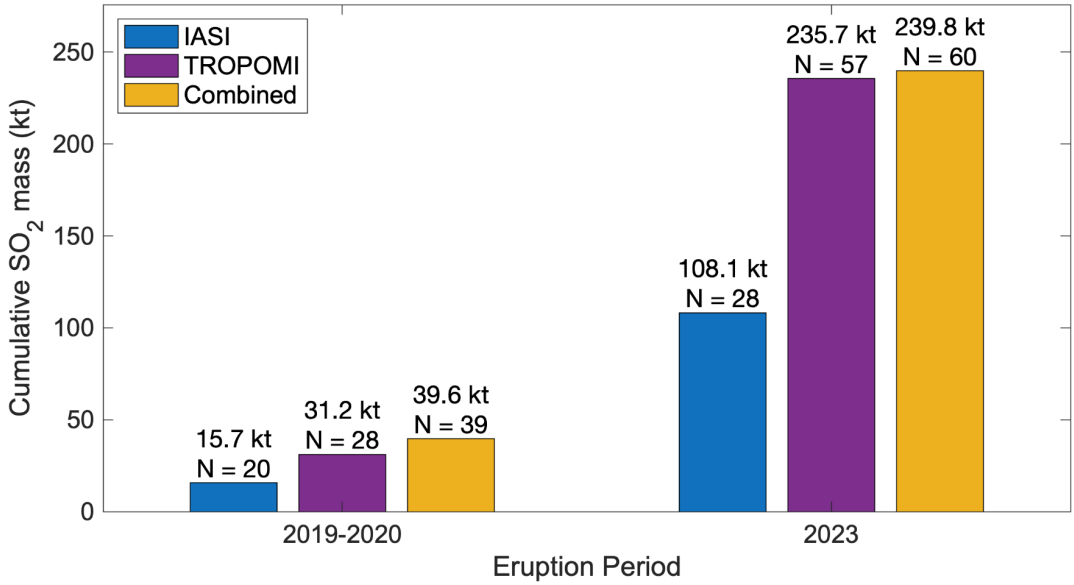


Figure S.4: Bar diagrams for the 2019–2020 (left) and 2023 (right) Shishaldin Volcano eruptions showing cumulative eruptive SO_2 mass determined from IASI only (blue), TROPOMI only (purple), and the best combined mass (largest per day) derived from either IASI or TROPOMI sensors (yellow). The number of detections (N) used to calculate the total masses and the total mass for each category are listed above their respective bars.

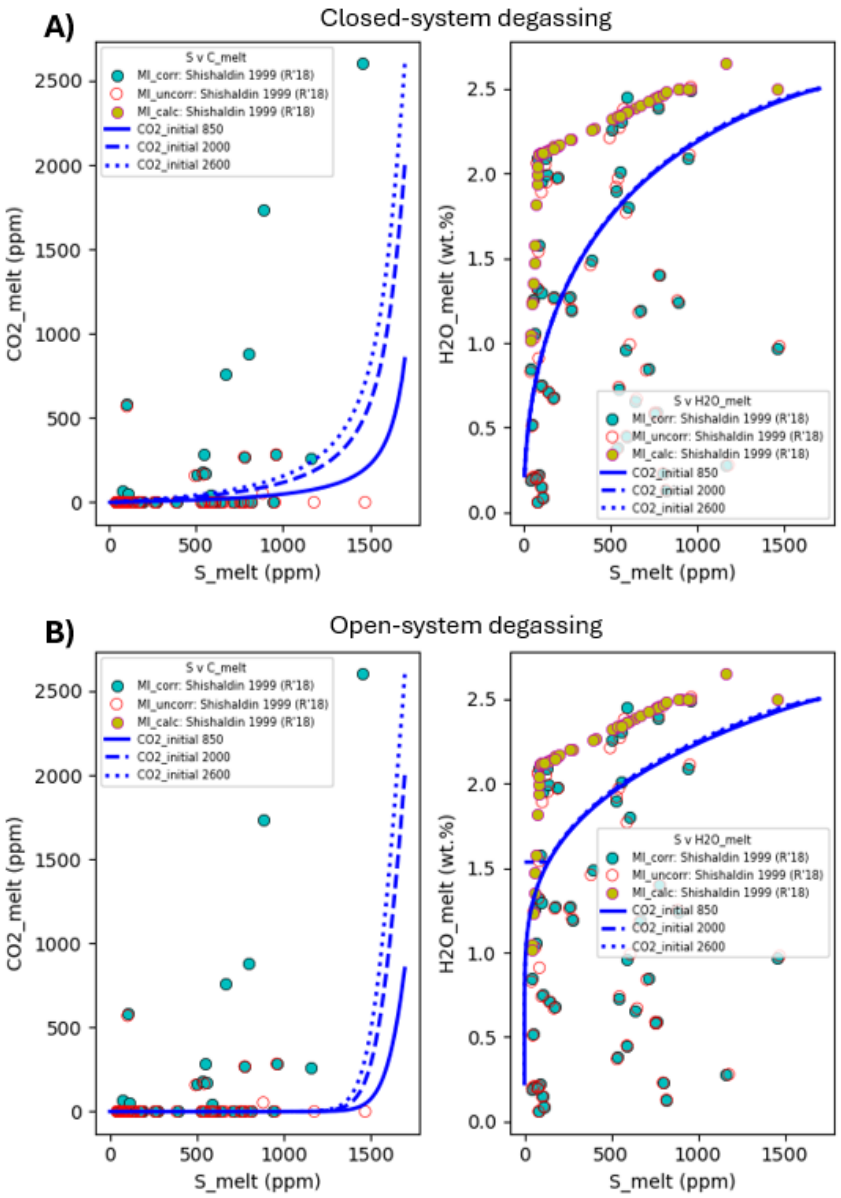


Figure S.5: Sulfur_X open-system (A) and closed-system (B) degassing model results (see Figs. 9, 10) of (left) S and CO_2 in the melt and (right) S and H_2O in the melt shown in blue. In both scenarios, the modeled melt is assumed to be 1120°C, fO_2 = FQM+0.9 (S^{6+}/S^{total} 0.3−0.4), and to initially contain 1710 ppm S and 2.5 wt.% H_2O. Three different initial CO_2 concentrations are modeled: 850, 2000, and 2600 ppm (respectively solid, long dashed, and dotted lines across all panels). Volatiles in melt inclusions from the Shishaldin Volcano's 1999 eruption (circles) measured by Rasmussen et al. (2018) are shown for comparison. Open circles are uncorrected melt inclusion measurements; filled green circles are post-entrapment crystallization-corrected melt inclusion concentrations; filled yellow circles are re-calculated H_2O values to account for diffusive H_2O-loss from the inclusions (see Rasmussen et al. (2018) for explanations).

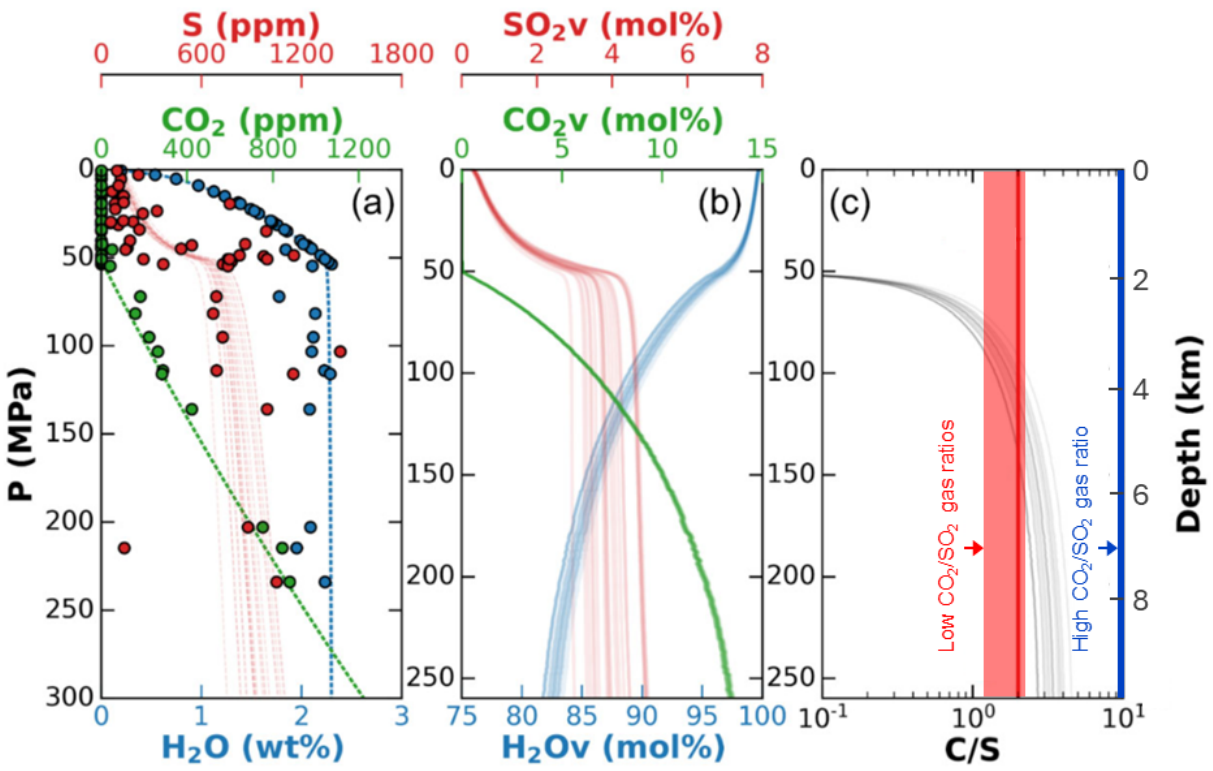


Figure S.6: Empirical degassing model fit to measured volatiles in melt inclusions from Shishaldin Volcano's 1999 eruption. A) Volatile concentrations measured in melt inclusions (circles) and the empirical degassing model result for remaining volatile species in the melt during magma ascent (curves). B) Modeled composition of the co-existing exsolving vapor during magma ascent. C) Modeled C/S ratios in the exsolved vapor, with ranges of low- and high-C/S gas measurements at Shishaldin Volcano indicated (red and blue bands, respectively). Initial volatile concentrations (2.3 wt.% H_2O, 1300 ppm CO_2) are based on analyses of primitive melt inclusions from the 1999 eruption (Rasmussen et al., 2018) and are similar to those presented in Figures 9 and 10 in the main text. Remaining S concentration in the melt is modeled and based on a K_2O-SO_2 regression of measured values (see Werner et al., 2020). Depth below the surface assumes a crustal rock density of 2700 kg/m^3.

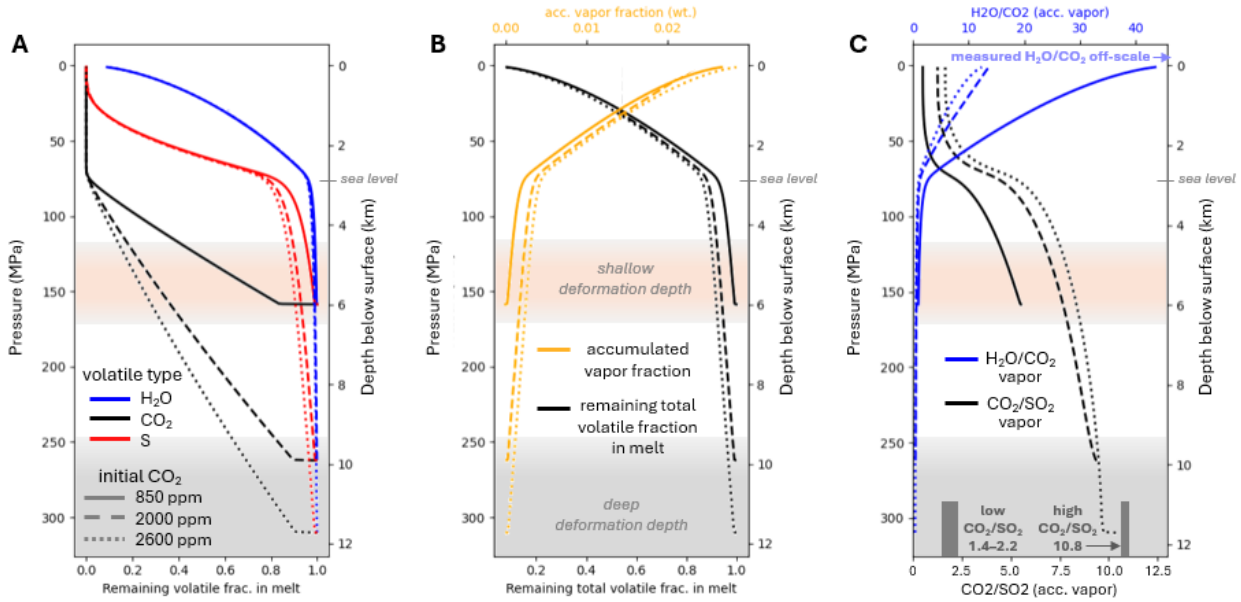


Figure S.7: Sulfur_X open-system isothermal degassing model for a Shishaldin basaltic melt using the CO_2-H_2O degassing model of Iacono-Marziano et al. (2012). Model conditions and figure symbology are the same as in Figs. 9 and 10 in the main text. Panel C shows CO_2/SO_2 and H_2O/CO_2 ratios of accumulated gas during open-system degassing behavior (compare to Fig. 10 of the main text, which shows instantaneous gas ratios for each pressure step). Airborne-measured gas compositions shown as bars along the bottom and top axes, with the measured H_2O/CO_2 ratio being off-scale (see Table 2). Depth below the surface assumes a crustal rock density of 2700 kg/m^3. Horizontal shaded regions indicate the approximate depth of the Shishaldin deformation sources (i.e., possible magma reservoirs) from Angarita et al. (2026a).